# Solution-Diffusion with imperfections model applied to fluorinated-liquid infused membranes

to obtain the degree of Bachelor of Science in Molecular Science and Technology at the Delft University of Technology

Endino Gieske

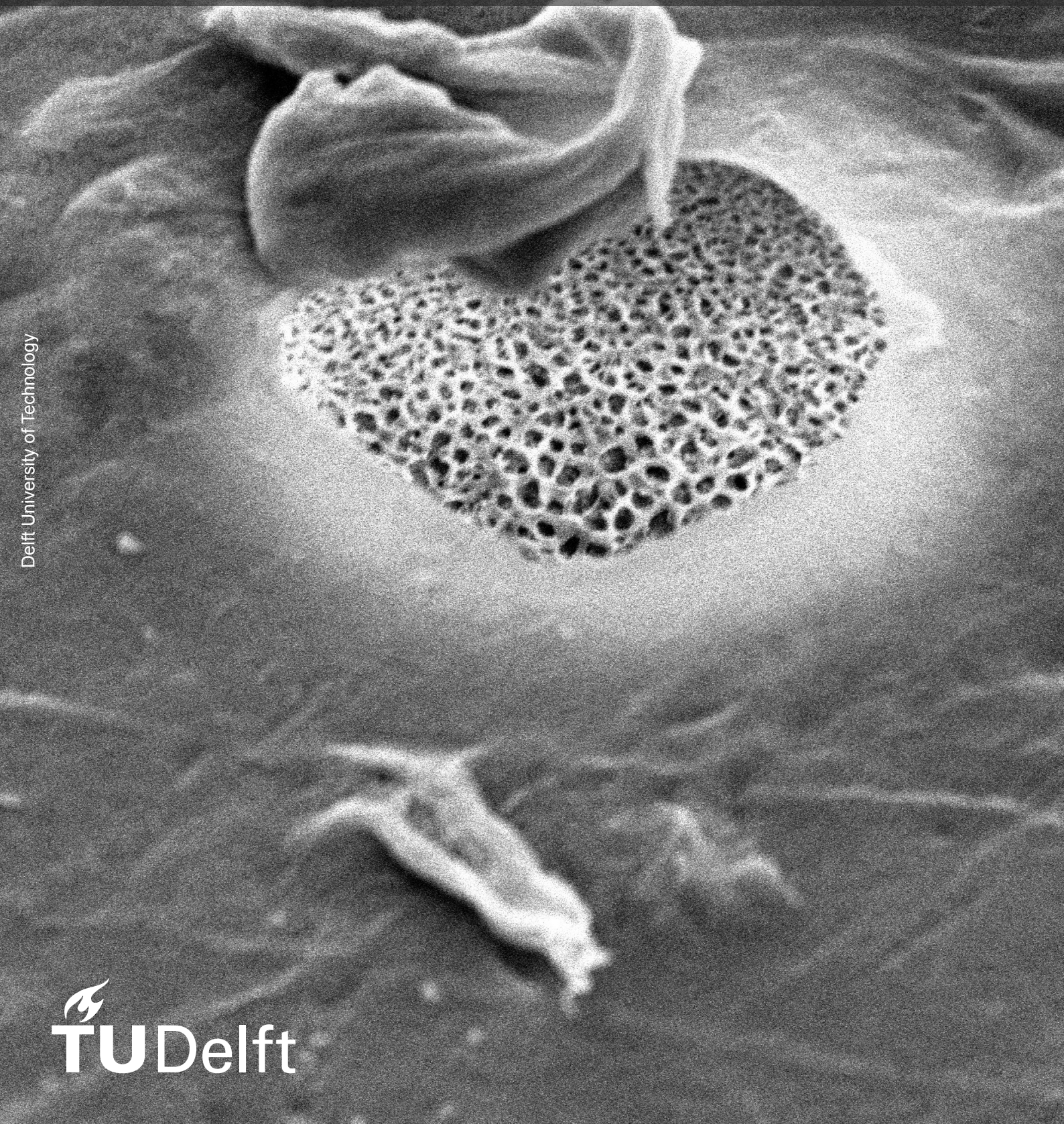

Delft University of Technology

TU Delft

# Solution-Diffusion with imperfections model applied to fluorinated-liquid infused membranes

to obtain the degree of Bachelor of Science in Molecular Science and Technology at the Delft University of Technology

by


| Student Name | Student Number |
|---|---|
| Endino Gieske | 5186137 |


| | |
|---|---|
| Daily supervisor: | H. Bazyar |
| Committee members: | H. Bazyar, A. Urakawa |
| Project Duration: | 25 April, 2022 - 14 July, 2022 |
| Faculty: | Process & Energy, Delft |

Cover: SEM Image of PVDF membrane synthesized by Combined Crystallization & Diffusion

TU Delft

# Abstract

Supported liquid membranes have recently attracted a lot of attention in the field of gas separation. They are an innovation upon membranes, having improved separation performance over conventional membranes. Typically, membranes are infused with non-volatile liquids such as ionic liquids or deep eutectic solvents. The liquids chosen typically are good solvents for certain gases such as carbon dioxide, therefore attention is put towards using supported liquid membranes as a carbon capture technology. Most supported liquid membranes follow the solution-diffusion model, meanwhile conventional porous membranes follow the pore-flow model. However, in special cases of organic solvent nanofiltration, the membranes are described by a combination of both models, the solution-diffusion with imperfections model. This work studies which model best applies to fluorinated liquid-infused membranes, known as slippery liquid-infused membranes, by measuring the permeability experimentally and comparing it with the theoretical permeability values obtained from experimental and theoretical solubility parameters.

# Contents


**Summary** i

**1 Introduction** 1

**2 Transport Model** 3

**3 Materials & Methods** 7

**4 Results & Discussion** 11

**5 Conclusion** 26

**6 Acknowledgements** 27

**A Appendix** 31

# 1 Introduction

The emergence of global warming has presented a large scale obstacle to overcome, with the world set on limiting global temperature rise to 1.5 °C [10]. The burning of fossil fuels for many processes emits greenhouse gases (GHG's) such as $CO_2$ into the atmosphere, which has destabilizing effects on the planet. The Intergovernmental Panel on Climate Change (IPCC) reported that approximately 41 billion tons of $CO_2$ are emitted annually [11]. With many processes transitioning to more sustainable alternatives, there is some hope that the global emission of GHG's will drop significantly. However, for essential processes where $CO_2$ emission is unavoidable, methods of capturing and storing $CO_2$ are necessary to avoid further increasing global temperatures. A way to store the carbon dioxide is by using electricity produced from solar panels or windmills and converting it into valuable chemicals such as methanol, dimethyl ether or higher order hydrocarbons [20][21]. This has led to a lot of research into capturing $CO_2$, which utilizes many processes such as adsorption, absorption, separation by membranes and chemical capture [32].

Membrane separation is a process where a material acts as barrier for one molecule, meanwhile it allows another molecule to permeate easily, allowing for separation of the two [3]. Separation can occur due to many factors, such as molecular size, electric charge, solubility etc. Many processes necessary for urban life use membrane separation such as drinking water generation. Sea water or brackish water is passed through a Reverse Osmosis (RO) membrane, and drinkable water comes out the other end. RO relies on the different permeabilities of water and salt in the membrane, allowing water to pass freely through the membrane and rejects 98% of the salts [3, 33]. Ultrafiltration, microfiltration and nanofiltration all separate by the difference in the size of molecules in the feed, allowing only molecules smaller than the pores of the membrane to permeate. The names related to the filtration depend on the pore size, ranging from millimeter scale to nanometers in diameter. Membranes are typically used in solid/liquid or liquid/liquid separation, membranes can also be used for gas/gas separation. This relies on the different permeabilities of the gases within the membrane, where permeability is a factor accounting for the ease at which the gas dissolves in the membrane and how quickly the dissolved gas diffuses through the membrane [35].

Separating $CO_2$ with the use of membranes is believed to be an attractive alternative to cryogenic distillation, adsorption onto solids or solvent absorption as these conventional processes are very energy intensive. Added to this, membrane technologies only require a small footprint, typically have lower capital expenditures, does not make use of phase changes, can be performed at low temperatures and the function of the membrane can be varied depending on the chosen material [3, 33]. Polymeric membranes such as cellulose acetate or polyimide membranes are typically used to separate $CO_2$ from natural gas streams, allowing it to be used for combustion. A lot of research is being done on designing better membranes for similar applications, however an issue with membranes is that as the permeability increases, the selectivity decreases and vice versa [24]. Selectivity is the preference of a membrane to allow a specific compound to permeate over another compound. This is known as the Robeson upper bound, this has been revisited in 2008 [25], which is shown graphically in Figure 1.1.

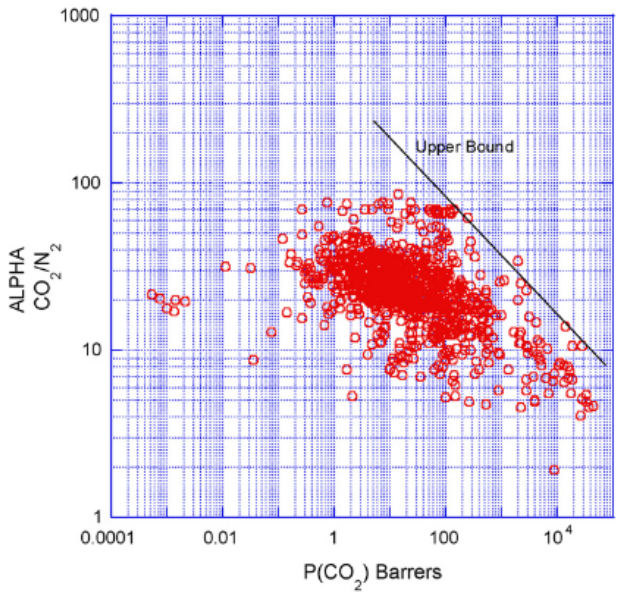


**Figure 1.1:** Robeson upper bound revisited. ALPHA stands for the selectivity of a membrane, in this case: $CO_2$ over $N_2$. $P(CO_2)$ is the permeability of $CO_2$ in the unit Barrer. Reproduced from "the upper bound revisited" by L.M. Robeson, 2008 1.1.

To push for high permeability and selectivity, liquid membranes have been devised, first thought of in 1967 by Ward and Robb to separate $CO_2$ from $O_2$ [34]. According to the Solution-Diffusion model, permeability should increase due to higher diffusive rates in a liquid. Liquid membranes are different than standard membranes used in the industry, because the membrane consists of a liquid phase rather than a porous or dense solid. A bulk liquid can act as the membrane, however, to make a mechanically stable membrane the layer must be thick, which leads to lower fluxes as membrane thickness is inversely proportional to flux. To overcome the thickness problem whilst retaining a single liquid phase as the membrane, Uchityl et al. came up with a dynamic liquid membrane that allows for a much thinner membrane thickness. A dynamic liquid membrane is a thin layer of liquid allowed to flow over a permeation cell containing a gas mixture, the gas permeates the thin liquid film and the liquid film is continuously regenerated via a pump, therefore described as dynamic [31].

Supported liquid membranes are a technology to create mechanically stable membranes with a small thickness. A supported liquid membrane such as immobilized liquid membranes (ILM's) typically consist of a liquid encased in a scaffold material, this scaffolding is made out of polymeric material that may have pores with liquid trapped in by capillary forces [14]. The liquid provides most of the separation performance, the polymeric scaffolding provides the mechanical support. Polymers are primarily used due to their low price and sturdiness. One large shortcoming of liquid membranes is that they are not stable due to the liquid evaporating or being forced out of the capillaries by the pressure forces. This has led to researchers searching for liquids with very low volatilities to prevent evaporative leakage. Ionic Liquids (IL's) have recently been researched thoroughly. IL's are salts in the liquid phase at room temperature with very low vapor pressures [26]. The characteristics and specifics of IL's in membranes is discussed in the extensive review by Fries et al. [9]. Very similar in composition as IL's, Deep Eutectic Solvents (DES) are also used in SLM's. DES are eutectic mixtures of two materials, primarily two organic salts [29]. The primary requirements of the liquid phase in an SLM that is non-volatile and is compatible with the polymeric matrix. More detailed advances on gas separation using SLM's is described by Krejca and Kocherginsky et al. [15, 13].

The objective of this thesis is to investigate the $CO_2$ transport of two flourinated oils (Krytox 101 [16], Krytox 102 [17]) impregnated in a porous polyvinylidene fluoride (PVDF) matrix. The real gas flow of $CO_2$ through these supported liquid membranes is measured. The solubility of $CO_2$ within the oils at low pressures is also explored to calculate the theoretical gas flow and is compared to the real gas flow.

# 2

# Transport Model

Gas transport through porous, dense and supported liquid membranes is primarily governed by two models, pore-flow and solution-diffusion model. The driving force in all separation is the chemical potential ($\mu$) gradient [35], which includes all other driving forces such as pressure, concentration, temperature and electrical potential gradients. As transport through membranes only occur in one direction, the flux of species $i$ is:

$$J_i = -L_i \frac{d\mu_i}{dx} \tag{2.1}$$

Where $L_i$ is a coefficient describing the mobility of species $i$ through the membrane and $\frac{d\mu_i}{dx}$ is the chemical potential gradient of species $i$ from the feed to the permeate side.
The chemical potential in conditions suited to typical membranes can be described as:

$$d\mu_i = RT \cdot d(ln(\gamma_i c_i)) + V_i dP \tag{2.2}$$

Where $R$ is the molar gas constant, $T$ is the temperature, $\gamma_i$ is the activity coefficient of $i$, $c_i$ is the molar concentration of $i$, $V_i$ is the molar volume and $P$ is the pressure. When using membranes, the driving forces are usually concentration and/or pressure gradients, therefore only these two are included in the formulation of the chemical potential $\mu_i$. It is assumed that species $i$ on either side of the membrane is in equilibrium with the membrane surface ($\mu_i^m = \mu_i$), therefore there is a continuous chemical potential gradient within the membrane [35].

**PORE-FLOW MODEL**
In porous membranes, gas molecules flow through the pores and follow the pore-flow model. The pore geometry and size can differ greatly between membranes, and therefore the pore-flow model is an overarching term for different models that all describe gaseous molecules flowing through membrane pores. The pore size determines the separation; from 0.1 to 10 $\mu$m, no separation occurs, all gas molecules simply flow through the membrane pores, known as convective flow (alternatively, viscous flow) [3]. With pore sizes smaller than 0.1 $\mu$m, the pores are similar or smaller than the mean free path of gas molecules (average distance taken between collisions). Separation occurs via effusion (Knudsen diffusion), which obeys Graham's Law of effusion. Effusion is slightly different from diffusion specifically in that the mean free path is larger than the pores, making transport different and making effusion inversely proportional to the square root of the molecular weight ($\propto \frac{1}{\sqrt{M_w}}$). When the pore sizes approach the diameter of gas molecules, range of 5-20 Å, separation occurs via a sieving effect which rejects larger molecules while allowing smaller molecules to effuse through the pores or adsorb onto the pore surface and diffuse through the pore [3].

Pore-flow models assume a uniform concentration of solute within the membrane, therefore the chemical potential is only influenced by the absolute pressure gradient [35] and equation 2.2 becomes:

$$\begin{aligned} d\mu_i &= V_i dP \\ \mu_i &= \mu_i^0 + V_i \triangle P \end{aligned} \tag{2.3}$$

With $\triangle P$ being the absolute pressure difference between the feed and permeate. $\mu_i^0$ is the chemical potential of pure $i$. Combining equation 2.1 and 2.3 yields:

$$J_i = -L_i V_i \frac{dP}{dx} \tag{2.4}$$

Equation 2.4 is another formulation of the well-known **Darcy's law** of convection [8]:

$$J_i = \frac{k_i^d}{\eta} \frac{\triangle P}{l} \tag{2.5}$$

With $k_i^d$ being the Darcy permeability coefficient (related to the porosity of the membrane), $\eta$ is the dynamic viscosity and $l$ is the membrane thickness. An expansion of Darcy's law is the **Hagen-Poiseuille equation**, which assumes cylindrical pores perpendicular to the membrane surface [36]:

$$J_i = \frac{\varepsilon r^2}{8\eta\tau} \frac{\triangle P}{l} \tag{2.6}$$

$\varepsilon$ is the porosity of the membrane, $r$ is the pore radius and $\tau$ is the tortuosity. The porosity $\varepsilon$ is the fraction of membrane volume inhabited by pores. The tortuosity $\tau$ represents the length of the average pore compared to the membrane thickness $l$. When the pores within the membrane direct themselves in all directions, it can be assumed that the tortuosity is approximately 3 (in many cases however, the membrane tortuosity is between 1.5 to 2.5, as the pores do not perfectly align themselves in 3 dimensions). Another expansion of Darcy's law is the **Carmen-Kozeny relation**, which assumes a porous media of packed spheres [23]:

$$J_i = \frac{\varepsilon^3}{K\eta A_p^2 \cdot (1-\varepsilon)^2} \frac{\triangle P}{l} \tag{2.7}$$

Here $K$ is the Carmen-Kozeny constant and $A_p$ is the internal surface area of the pores. Both the Hagen-Poseuille and Carmen-Kozeny describe pore-flow when the pore diameter is much larger than the mean free path ($\lambda$), also known as convective flow:

$$\lambda = \frac{k_b T}{\sqrt{2}\pi d_i^2 P} \tag{2.8}$$

$P$ is the pressure within the membrane pore, $k_b$ is Boltzmann's constant and $d_i$ is the kinetic diameter. When the mean free path is considerably larger than the pore diameter, pore-flow can be described by **Knudsen diffusion** [19]:

$$\begin{aligned} J_i &= \frac{D_{i,K}}{RT} \frac{\triangle P}{l} \\ D_{i,K} &= \frac{\varepsilon \cdot r}{3\tau} \sqrt{\frac{2RT}{\pi M_w}} \end{aligned} \tag{2.9}$$

$D_{i,K}$ is the Knudsen diffusion coefficient including both the porosity and tortuosity. For binary mixtures, **Graham's law** of effusion can be used, where the fluxes of both compounds are related:

$$\frac{J_i}{J_j} = \sqrt{\frac{M_{w,j}}{M_{w,i}}} \tag{2.10}$$

When two gas molecules of different species permeate through very small holes (pores), the rate of effusion of the two are related to each other and their molar masses. The heavier the gas molecule, the slower it will effuse through the pores, leading to lower fluxes of one species and this leads to separation.

**SOLUTION-DIFFUSION MODEL**

In dense and supported liquid membranes, separation is described by the solution-diffusion model. This is a process where a molecule dissolves onto the membrane surface, diffuses through the matrix

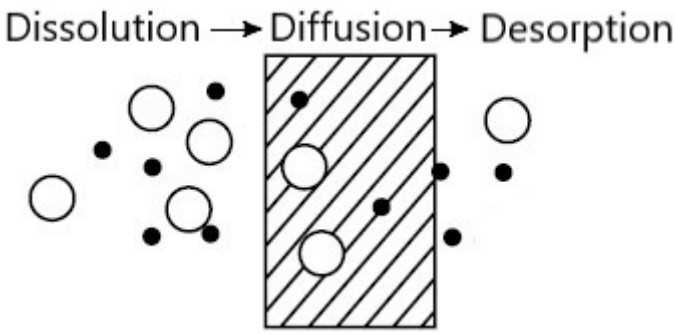


**Figure 2.1:** Solution-diffusion mechanism. First the molecule dissolves into the membrane, diffuses to to the side of the membrane and then desorbs from the membrane. Reproduced and modified from Membrane Technology and Applications 2nd edition by Richard W. Baker

to the other end and then desorbs from the membrane surface, schematically shown in Figure 2.1. Separation occurs in the rate of dissolution/desorption and the rate of diffusion. The larger the molecule, the more readily it will dissolve. However, the smaller the molecule, the easier it will diffuse through the membrane matrix. The type of membrane will prefer one process (sorption or diffusion) over the other, and will separate the molecules based on these characteristics [35].
The solution-diffusion model assumes no pressure difference within the membrane, leading to the chemical potential with concentration as the driving force:

$$\begin{aligned} d\mu_i &= RT \cdot d(ln(\gamma_i c_i)) \\ \mu_i &= \mu_i^0 + RT \cdot ln(\gamma_i c_i) \end{aligned} \tag{2.11}$$

Combining equation 2.1 and 2.11 yields **Fick's first law** of diffusion, where the concentration gradient is the driving force [35]:

$$\begin{aligned} J_i &= -D_{i,F} \frac{dc_i}{dx} \\ J_i &= -D_{i,F} \frac{\triangle c}{l} \end{aligned} \tag{2.12}$$

$D_{i,F}$ is Fick's diffusion coefficient and the latter equation is an application of Fick's first law onto membranes, with $\triangle c = c_{i,P}^m - c_{i,F}^m$ which is the concentration difference between the permeate and the feed side on the membrane surface, respectively. Combining equation 2.11 and our previous assumption of equilibrium on the membrane surface with the feed/permeate ($\mu_i^m = \mu_i$) leads to equation 2.13, which can then be reduced to equation 2.14 [35]:

$$\mu_i^0 + RT \cdot ln(\gamma_i^m c_i^m) = \mu_i^0 + RT \cdot ln(\gamma_i c_i) \tag{2.13}$$

$$c_i^m = \frac{\gamma_i}{\gamma_i^m} c_i \tag{2.14}$$

The ratio between the activity coefficients of the feed/permeate and membrane surface is known as the **sorption coefficient** $K_i$, alternatively known as the solubility:

$$\begin{aligned} K_i &= \frac{\gamma_i}{\gamma_i^m} \\ c_i^m &= K_i c_i \end{aligned} \tag{2.15}$$

Filling in equation 2.15 into Fick's first law of diffusion (equation 2.12):

$$\begin{aligned} J_i &= \frac{-D_i K_i}{l}(c_{i,P} - c_{i,F}) \\ J_i &= \frac{Pe_i}{l}(c_{i,F} - c_{i,P}) \\ J_i &= \frac{Pe_i}{l}(p_{i,F} - p_{i,P}) \end{aligned} \tag{2.16}$$

In cases of gas separation, the partial pressures $p$ can be used instead of the concentration. $Pe_i$ is known as the **permeability** of a membrane [3], which is the product of the diffusion coefficient $D_i^F$ and the sorption coefficient $K_i$. The permeability depends on the type of membrane used and which species is to permeate the membrane. The **selectivity** $\alpha_{i/j}$ of a membrane is the ”preference” of a membrane to permeate species $i$ over $j$, mathematically noted as:

$$\alpha_{i/j} = \frac{Pe_i}{Pe_j} \tag{2.17}$$

Considering the permeability $Pe$ is dependent on which species are present in the feed, the feed composition will change the selectivity $\alpha_{i/j}$ as well. In literature, the ideal selectivity is usually measured, which uses the permeability measured of only one species. The ideal selectivity can lead to incorrect assumptions about a system, therefore the real selectivity is necessary. This is measured using a binary mixture of species $i$ and $j$, where different ratio's of the mixture leads to different real selectivities. Real selectivities are typically smaller than ideal selectivities, as $i$ can interact with the membrane sufficiently to allow an increased permeability of $j$ (e.g. the dissolution of $i$ can lead to the polymer within the membrane to swell, changing the structure, leading to change an increase in permeability of $j$).

**SOLUTION-DIFFUSION WITH IMPERFECTIONS MODEL**

In cases where the pores are not large enough to be described by the pore-flow model, yet there are small pores present which doesnt allow the membrane to be fully described by the solution-diffusion model, a new model was devised by combining the two [8]. This is termed as the Solution-Diffusion with imperfections model, where compounds permeate the membrane by sorption and diffusion and also by convection or Knudsen diffusion through pores, first thought of by Sherwood et al. [28]. The flux thus has terms of both the solution-diffusion model and pore-flow model:

$$J_i = J_{SD} + J_{PF} \tag{2.18}$$

If convective flow is present due to cylindrical shaped imperfections in the membrane, the flux can be described using equations 2.6 and 2.16:

$$J_i = Pe_i \frac{\triangle p}{l} + \frac{\varepsilon \cdot r^2}{8\eta\tau} \frac{\triangle P}{l} \tag{2.19}$$

If the pores are small enough, Knudsen diffusion takes place and the flux can be described by:

$$J_i = Pe_i \frac{\triangle p}{l} + \frac{D_{i,K}}{RT} \frac{\triangle P}{l} \tag{2.20}$$

# 3

# Materials & Methods

**MATERIALS**

The porous membranes were created by the Combined Crystallization & Diffusion (CCD) method [27]. This was done by Dr. V. Shah at the Department of Chemical Engineering at Imperial College London. This method is shown in Figure 3.1.

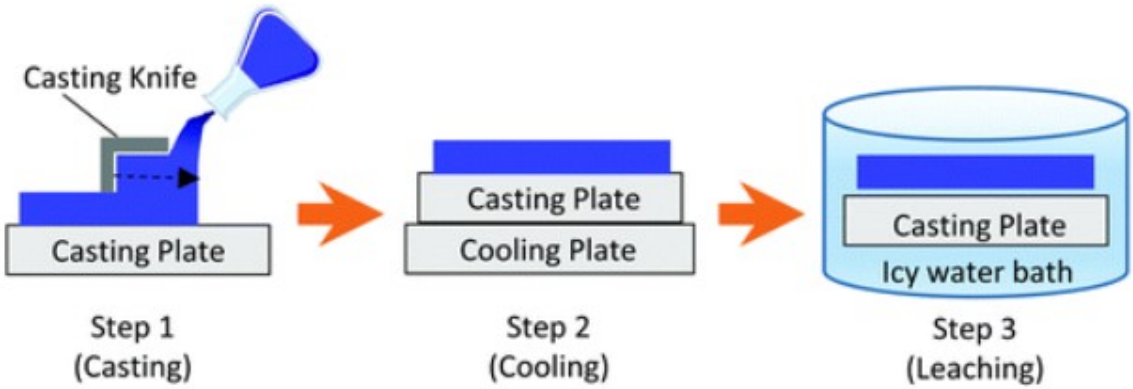


**Figure 3.1:** Schematic representation of the Combined Crystallization & Diffusion method. A layer of polymer solution is cast onto a aluminum plate (Step 1), where this plate was set ontop of a cold aluminum plate precooled to -30 °C (Step 2) and lastly the solvent within the solidified membrane was leached out in an icy water bath (Step 3). Reproduced from "High-performance PVDF membranes prepared by the combined crystallisation and diffusion (CCD) method using a dual-casting technique: a breakthrough for water treatment applications" by Shah et al., 2021

Two sets of membranes were made, one with smaller pores than the other. In this article they are referred to as **CCD** for the larger pore sized membrane and **CCDs** (CCD small) for the smaller pore sized membrane. The liquids used are fluorinated oils Krytox GPL 101 & Krytox GPL 102 [16, 17].

**MEMBRANE CHARACTERIZATION**

SEM imaging was performed on the top, bottom and cross section of the membrane using JEOL JSM-6010LA. All 3 sides were coated with gold layer by a JEOL JFC-1300 auto fine coater prior to the SEM analysis (settings were set at; 40s and 20 mA). The cross-sectional area was laid bare by dipping the membrane in liquid nitrogen, embrittling the membrane and thereby fracturing it. Infusion of the oil (Krytox 101 or Krytox 102) within the membrane was done by covering the membrane with the oil in a petri-dish with a pipette until a small layer of oil formed on top of the membrane. The ensure proper infusion, small droplets were also drippled around the membrane and allowed to rest for a minimum of 2 hours. The contact angle was measured using milli-Q water and an OCA 25 by DataPhysics Instruments. The dynamic contact angle was allowed to run for six cycles and the static contact angle

was measured 6 times at different locations atop the membrane. The surface tension of Krytox 102 was measured using the pendant drop method with the OCA 25 [5]. The pore size distribution was measured using Capillary Flow Porometry by an external company POROMETER based in Germany & Belgium [22].

**GAS SEPARATION EXPERIMENTS**

The gas separation experiments were performed using an in-house setup, schematically shown in Figure 3.2. The flow rate of the feed is controlled by mass flow controllers, which is brought through a convection oven and makes contact with the membrane. The retentate is then led to a back pressure regulator, which can modulate the pressure of the feed by way of a valve that is controlled by turning a knob. The back pressure regulator has a range of 1 to 10 bar. The permeate is carried to the detector by He/Ar sweep gas at atmospheric pressure, where the permeate is then analyzed by Gas Chromatography (CompactGC$^{4.0}$, Global Analyser Solution). He is used for all gases as a sweep gas, however in the case of $H_2$ analysis, Ar should be used as $H_2$ and He have very similar retention times and therefore are difficult to gather accurate results.

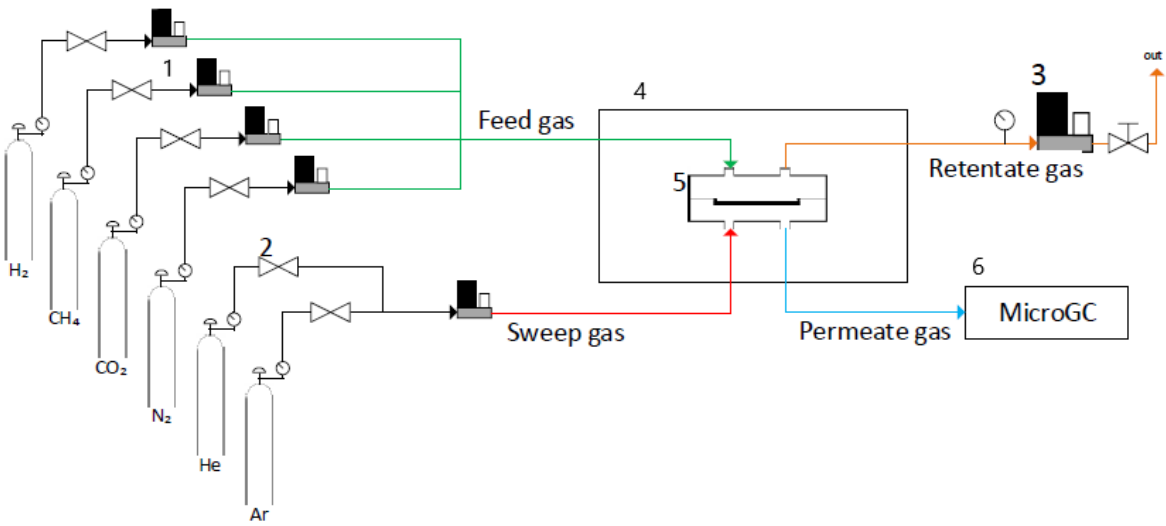


**Figure 3.2:** Schematic representation of the in house experimental setup for gas permeation. It consists of (1) mass flow controllers, (2) sweep gas valves, (3) back pressure regulator with valve, (4) temperature controlled oven, (5) membrane permeation cell and (6) GC setup. Reproduced from "Towards the next generation of supported liquid membranes for CO2 capture" thesis by G.J.A. Hooijer, 2021.

Calibration of the mass flow controllers and GC are necessary for proper feed flow rate control and permeate concentration calculation. The mass flow controllers were calibrated by setting the mass flow at a given flow rate (known as set point), and then measuring the real flow rate with a flow rate meter. This was done at several set points. The set point and real flow were then found to have a linear relationship, which was used to determine what set point is necessary to acquire the desired real flow rate. The chosen real flow rate for all experiments are 10 mL min$^{-1}$ for the feed and 5 mL min$^{-1}$ for the sweep gas. Pressure stability tests are performed by steadily increasing the relative pressure at 30 °C. The minimum accurate pressure allowed by the setup is 0.2 bar, therefore starting at 0.2 bar, the pressure is increased once steady state flux has been achieved at increments of 0.1 bar or more. An indicator of steady state flux is a relatively constant concentration readout from the GC for a minimum of 3 injections. The flux was measured by using the average concentration data upon steady-state. The breakthrough pressure is observed when a sudden and dramatic increase in flux is observed, which signifies the largest pores being opened and the oil being pushed out.
More information regarding some of the earlier discussed techniques is given in the Appendix.

**$CO_2$ SOLUBILITY EXPERIMENTS**

The solubility of $CO_2$ in Krytox 101 and Krytox 102 was measured using an in-house setup schematically shown in Figure 3.3. The setup is a variation of the pressure decay method (alternatively known as pressure drop) that is used by Mei et al. and Akbari & Valeh-e-Sheyda [18, 1]. The solubility is obtained by measuring the difference in gaseous $CO_2$ present in a system before and after having the $CO_2$ come in contact with the liquid. The main difference with our set-up is that first gas is injected into the vessel, where temperature and pressure are measured, and afterwards the liquid is injected via a syringe. The general procedure is to draw a vacuum in the vessel, which has been cleaned of any liquids. Afterwards the vessel is filled with $CO_2$ up to atmospheric pressure or higher, and then a vacuum is drawn once more. This is repeated once more to ensure almost no other gases are present in the vessel. The $CO_2$ is then injected to the desired temperature and allowed to equilibriate with the impeller spinning. Upon equilibriation, the pressure and temperature are noted as the initial pressure ($P_0$) and temperature ($T_0$). Then, the syringe with a known quantity of liquids injects the liquid into the vessel via the septum, and the pressure and temperature in the vessel are recorded throughout the entire experiment up to thermodynamic equilibrium. The impeller is used to speed up the process of equilibriation. A sign of equilibrium is a constant temperature and pressure of 30 or more minutes.

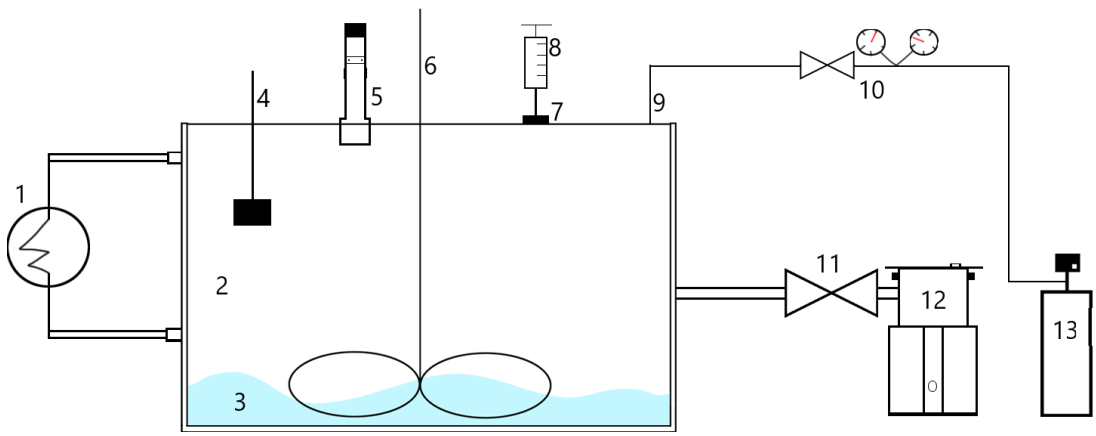


**Figure 3.3:** Solubility setup used for measuring $CO_2$ solubility in Krytox 101 and Krytox 102. It consists of (1) a heating element to control the vessel temperature, (2) vessel surrounded by a heating jacket connected to the heating element, (3) liquid which is to dissolve gas, (4) temperature sensor, (5) pressure sensor, (6) impeller connected to rotor, (7) septum, (8) needle which contains the liquid that is injected, (9) gas injection port, (10) valve and pressure regulator, (11) valve, (12) vacuum pump and (13) pressurized $CO_2$ cylinder.

As the initial pressure ($P_0$) and temperature ($T_0$) and reactor vessel volume ($V_0$) are known, the initial amount of $CO_2$ can be calculated using the ideal gas law for absolute pressures of 1 bar and lower:

$$n_0 = \frac{P_0 V_0}{R T_0} \tag{3.1}$$

After having injected liquid of volume $V_l$, measuring the temperature and pressure over time allows you to know the exact amount of $CO_2$ ($n_t$) that has yet to be absorbed by the liquid. Substracting the initial amount of $CO_2$ with the remaining $CO_2$, the amount of absorbed $CO_2$ ($n_{abs}$) can be attained:

$$\begin{aligned} n_t &= \frac{P_t(V_0 - V_l)}{R T_t} \\ n_{abs} = n_o - n_t &= \frac{P_0 V_0}{R T_0} - \frac{P_t(V_0 - V_l)}{R T_t} \end{aligned} \tag{3.2}$$

The obtained values are then converted to molar fractions, plotted against the absolute pressure of the gas and fitted with a second order polynomial, where the Henry's constant was obtained by calculating the slope as the molar fraction approaches zero, mathematically shown as [2]:

$$k_H = \lim_{x_i \to 0} (\frac{P}{x_i}) \tag{3.3}$$

Possible improvements to this setup are given in the last section of the Appendix.

**$CO_2$ SOLUBILITY VIA PC-SAFT MODELLING**

PC-SAFT (perturbed chain-statistical associating fluid theory) was used to model the low pressure solubility of $CO_2$ in Krytox 101 and Krytox 102 at 30 °C. This modelling was done by Thijs van Westen from the Institute of Thermodynamics and Thermal Process Engineering at the University of Stuttgart. The PC-SAFT model assumes molecules as hard chains, which can closely resemble polymers, and uses perturbation theory to calculate the interactive forces between the molecules. The parameters used in this model (chain length m, segment size $\sigma$, energy parameter $\epsilon$ and binary interaction parameter $k_{ij}$) were fitted to the compressed liquid densities of Krytox oils and the fugacity of $CO_2$ in equilibrium with Krytox 101 and Krytox 102.

# 4

# Results & Discussion

**Membrane Characterization**

Figure 4.1 shows the SEM images of the CCD membrane at different angles. The membrane consists of two sides with differing characteristics, namely one side being much more porous (Fig. 4.1A & 4.1B) and the other much more dense (Fig. 4.1C & 4.1D). However, even within the dense side there are still small pores present (at very high magnifications, now easily visible in the supplied images) and even small defects on the surface, an example of which is in the top middle section of Figure 4.1D. The pores on the porous side (Fig. 4.1B differ greatly in geometry from the pores on the dense side (Fig. 4.1C). The defects present within the membrane have likely occurred during synthesis and can pose an issue with the breakthrough pressure, as the defects are likely to be the largest pores and therefore the first pores to be opened.

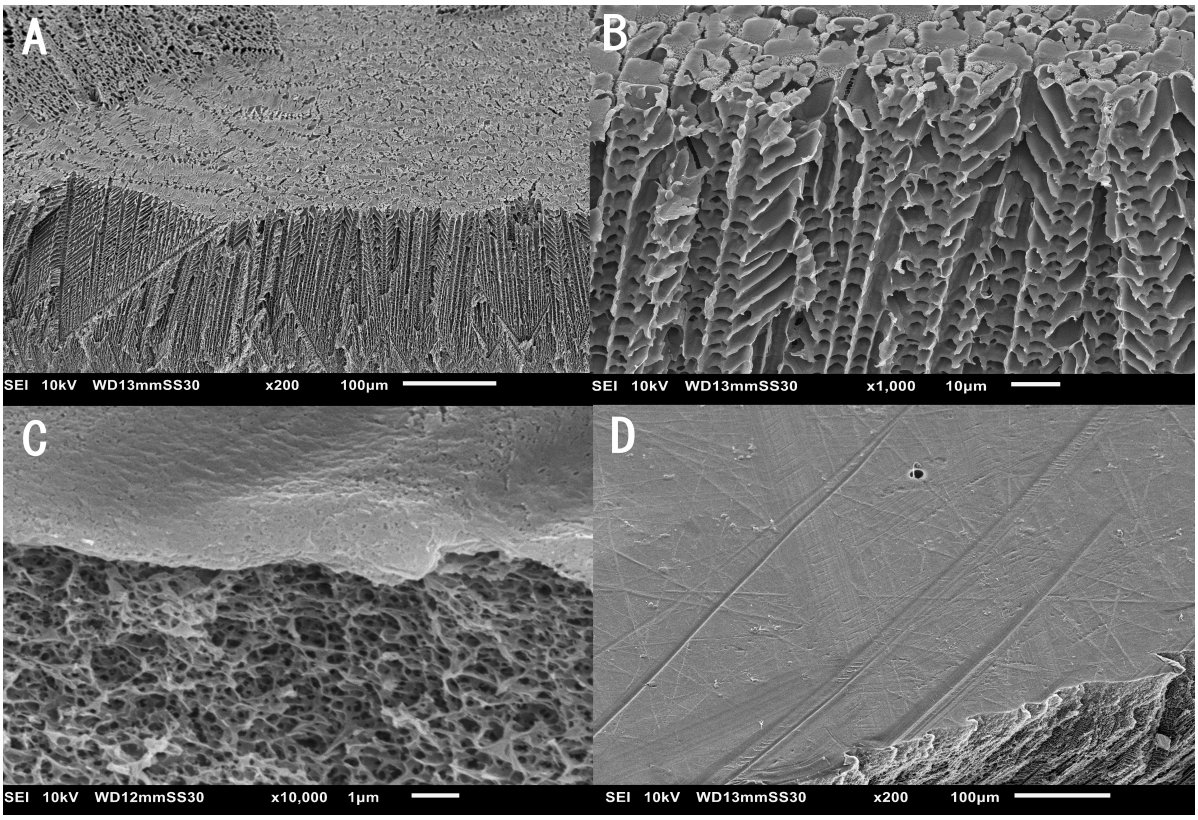


**Figure 4.1:** SEM images of the CCD membrane. A; Top & cross-sectional view on the porous side. B; Cross-sectional view of the porous side. C; Top & cross-sectional view of the dense side. D; Top view of the dense side, with a small defect visible in the middle top section.

In Figure 4.2 the SEM images of the CCDs membrane at different angles are shown. Similar to the CCD membrane, the CCDs membrane also consists of a porous and dense side. However, the pores on both sides do not differ drastically in geometry, only in size (Fig. 4.2B & 4.2D). Defects are also present within this membrane, visible for example as a tear through the surface in Figure 4.2A. The indentation visible on the left of 4.2A was made by grabbing the membrane with some tweezers. 4.2C shows the dense side at very high magnification (5000x), which shows visible pores on the surface of the membrane. These defects and pores on top of the surface are most likely the first failure points of the membrane and will be the first pores to be have the oil pushed out of.

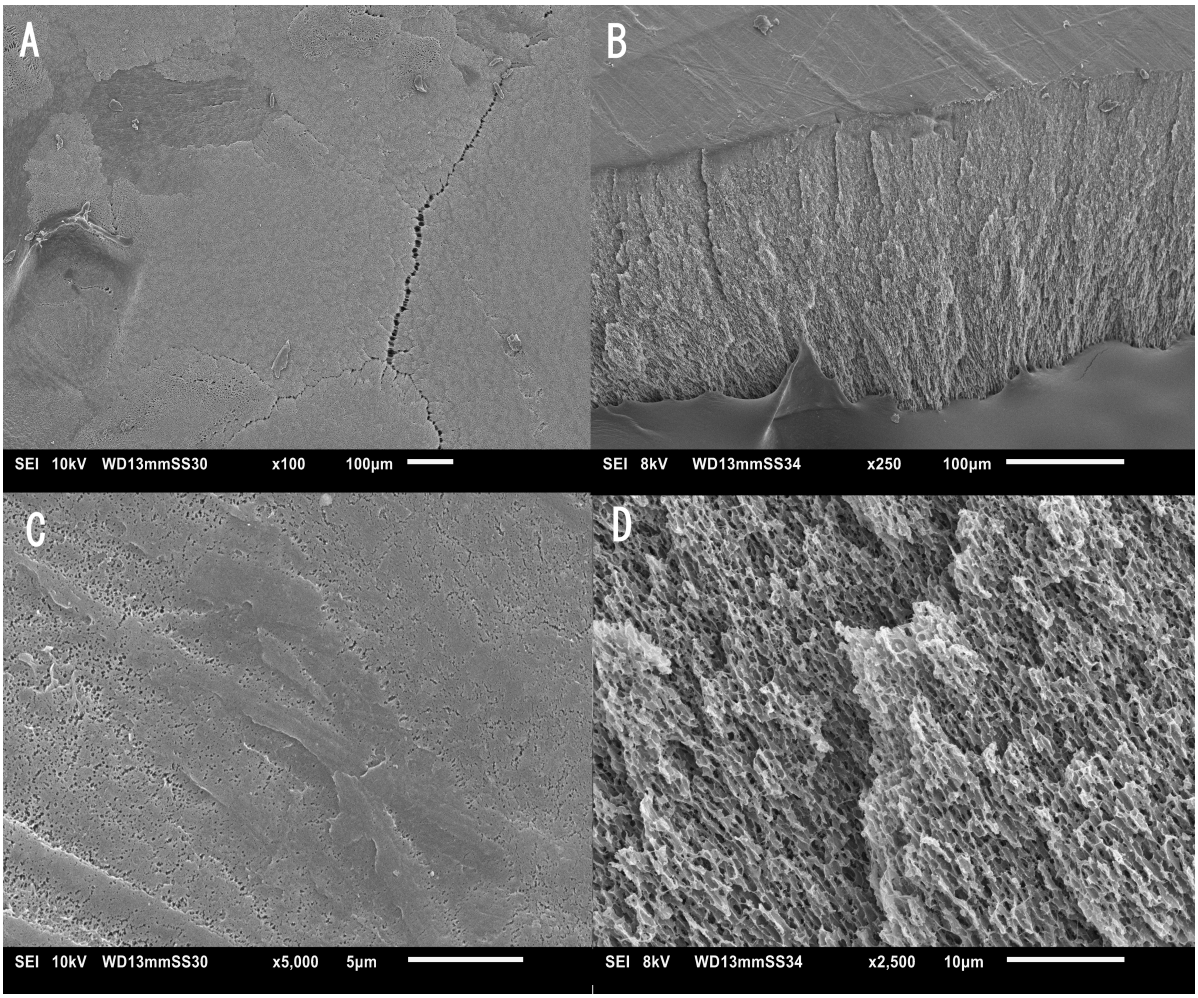


**Figure 4.2:** SEM images of the CCDs membrane. A; Top view on the porous side, a large tear through the membrane is visible. B; Cross-sectional view of the entire membrane & top view of the dense side. C; Top view of the dense side. D; Cross-sectional view of the dense side.

The membrane thickness of CCD and CCDs are 199 $\mu$m and 189 $\mu$m respectively. The capillary flow porometry results acquired from POROMETER are shown in Figure 4.3 & 4.4, the shaded region representing the standard deviation of 3 experiments. The pore size distribution attained from this further accentuates the fact that the membranes are not homogeneous. It should be noted that the pore size is the pore diameter. As shown in Figure 4.5, 3 runs were done on 3 samples of the CCD membrane. The result of first run differs significantly from the following two runs, it has a much higher peak percent flow which is also at a much smaller diameter than the two other runs. The results of run 2 & 3 are averaged out, shown in Figure 4.6 as the average pore size distribution, with the shaded region being the error. The CCDs membrane was similar with it having differing results, shown in Figure 4.7. The average pore size distribution was done using the two runs that were most similar to each other, shown in Figure 4.8.

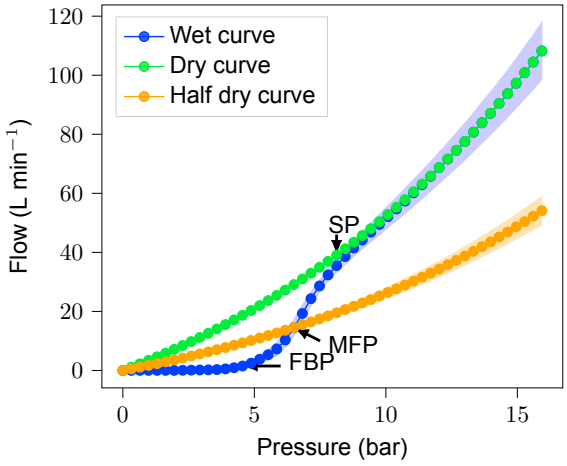


**Figure 4.3:** Capillary flow porometry results of the CCD membrane. The flow rate of nitrogen gas is plotted against the pressure. Shaded region shows the standard deviation. First Bubble Pore (FBP) = 275.13 $\pm$ 22.15 nm, Mean Flow Pore (MFP) = 92.54 $\pm$ 15.79 nm and Smallest Pore (SP) = 51.32 $\pm$ 9.81 nm.

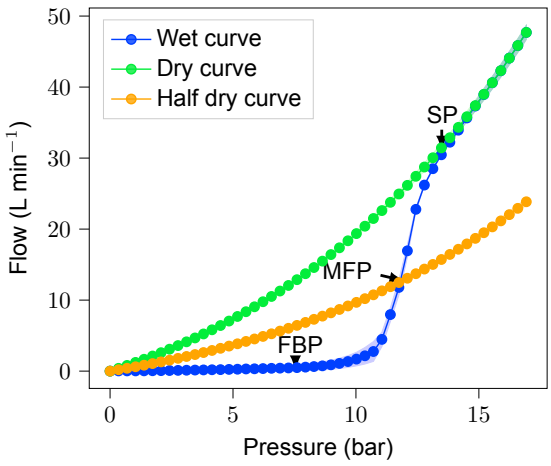


**Figure 4.4:** Capillary flow porometry results of the CCDs membrane. The flow rate of nitrogen gas is plotted against the pressure. Shaded region shows the standard deviation. First Bubble Pore (FBP) = 84.46 $\pm$ 0.84 nm, Mean Flow Pore (MFP) = 54.74 $\pm$ 2.06 nm and Smallest Pore (SP) = 44.30 $\pm$ 2.03 nm.

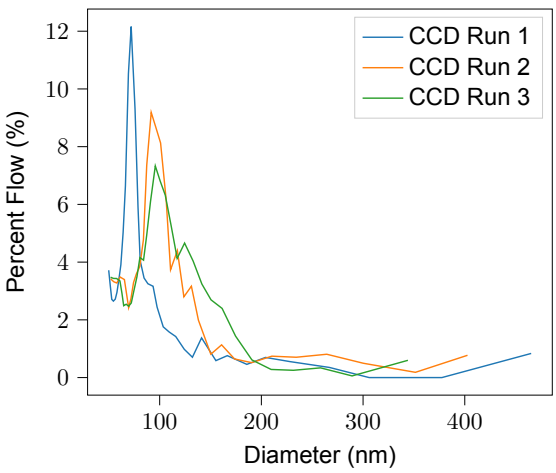


**Figure 4.5:** Pore size distribution of 3 different samples of the CCD membrane.

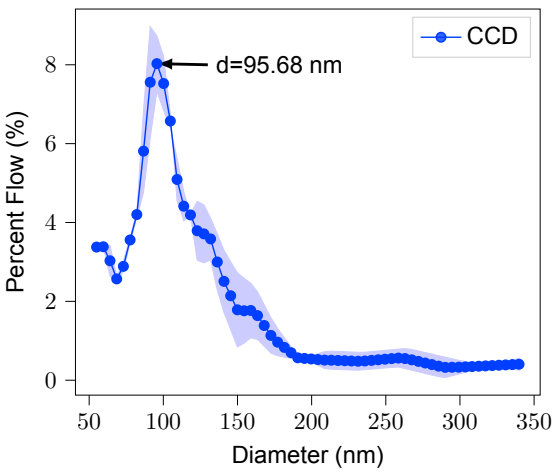


**Figure 4.6:** Average pore size distribution of the CCD membrane using run 2 & 3. Shaded region shows the standard deviation. Pore size attributed to peak is d = 95.68 nm.

**Table 4.1: Contact angles of the CCD and CCDs membrane without oil (dry), infused with Krytox 101 and infused with Krytox 102.**

| Contact Angles | Static (°) | Advancing (°) | Receding (°) | Hysteresis (°) |
|---|---|---|---|---|
| CCD dry | 96.81 $\pm$ 2.53 | 103.079 $\pm$ 0.369 | 47.17 $\pm$ 0.41 | 55.91 |
| CCD 101 | 107.33 $\pm$ 3.28 | 112.16 $\pm$ 1.23 | 57.05 $\pm$ 0.66 | 55.11 |
| CCD 102 | 109.15 $\pm$ 2.28 | 113.11 $\pm$ 0.77 | 74.32 $\pm$ 0.43 | 38.79 |
| CCDs dry | 106.70 $\pm$ 0.70 | 110.75 $\pm$ 0.86 | 63.07 $\pm$ 1.20 | 47.68 |
| CCDs 101 | 111.62 $\pm$ 1.77 | 112.14 $\pm$ 1.14 | 63.27 $\pm$ 3.01 | 49.07 |
| CCDs 102 | 111.37 $\pm$ 1.51 | 112.47 $\pm$ 0.63 | 72.24 $\pm$ 1.20 | 40.23 |

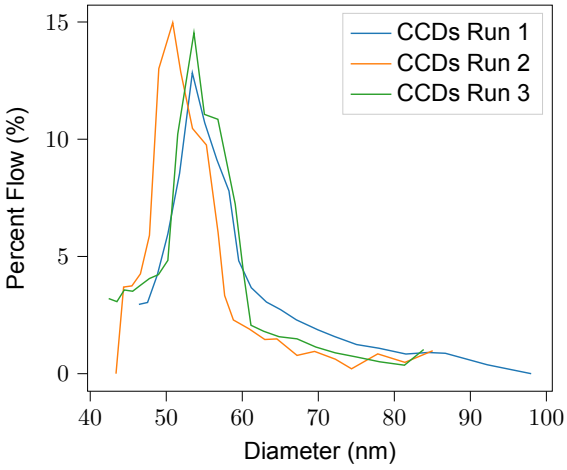


**Figure 4.7:** Pore size distribution of 3 different samples of the CCDs membrane.

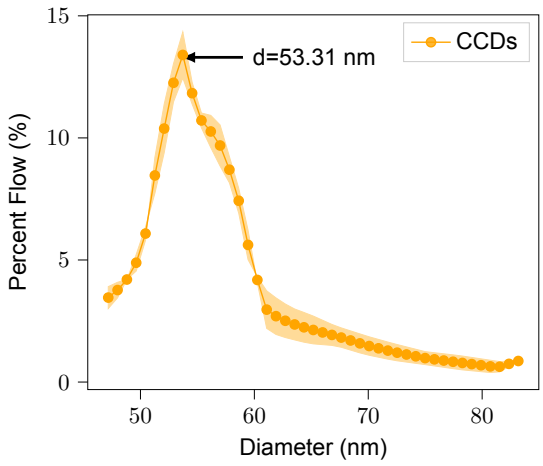


**Figure 4.8:** Average pore size distribution of the CCDs membrane using run 1 & 3. Shaded region shows the standard deviation. Pore size attributed to peak is d = 53.31 nm.

The contact angles of all variations of the membrane and oil mixtures are given in Table 4.1. The membranes are slightly hydrophobic (>90°), and becoming even more hydrophobic upon infusion with the oils. Something of note is the large hysteresis, which is the difference between the Advancing and Receding contact angle. A low hysteresis ($\approx 5°$) indicates slipperiness [4]. All the variations of the membranes used are not slippery and have a hysteresis above 40°. This could be due to additives used in the manufacturing of the membrane and/or due to bare membrane not being hydrophobic enough. Using the Young-Laplace equation (equation 4.1), the breakthrough pressure of the membranes can be calculated. This is when the pressure becomes large enough it will push out the oils out of the pores.

$$\triangle P = \frac{2\gamma \cdot \cos(\theta)}{r} \tag{4.1}$$

$\gamma$ is the surface tension of the oil, more explanation on the Young-Laplace equation is given in the appendix. Krytox 101 was reported to have a surface tension of 16.3 $\pm$ 0.13 mN m$^{-1}$ by Bazyar et al. [4]. The surface tension of Krytox 102 was measured by the pendant drop method to be 15.35 $\pm$ 0.18 mN m$^{-1}$.

**GAS SEPARATION EXPERIMENTS**

Before discussing the results of the gas separation experiments, it is important to discuss the possible ways errors can occur in the data. The first of which has already been discussed, that being the inhomogeneities within the membrane. Using different sections of the membrane can yield different results especially in the case of the breakthrough pressure. The second cause of error has to do with the mass flow controllers (MFC's) possibly being influenced by the environment. Daily factors such as humidity, temperature and pressure fluctuations can slightly influence the real flow rate of the MFC's. This can in theory be circumvented by calibrating the MFC's on a daily basis, however this is not practical. Therefore performing an experiment on one day can have different results on another day due to this error. The third way errors can occur is the back-pressure regulator. Back-pressure regulators are typically knobs that are turned to increase the pressure of the feed, and if it is coupled with a digital sensor with an output that is only a single decimal, it is very easy to choose the incorrect pressure. If the pressure sensor indicates the absolute feed pressure is 1.5 bar, it could mean that the absolute feed pressure is 1.51 bar or 1.59 bar. This can be circumvented by using an analog pressure sensor or with a high accuracy pressure sensor. However, the former allows for visuals errors and the latter will still suffer from the issue that analog pressure regulators are very sensitive and make it difficult to acquire the needed pressure.

Single and mixed gas experiments were performed on the CCD membrane infused with Krytox 101 using both $CO_2$ and $N_2$ gas, shown in Figure 4.9 & 4.10, with the flux being plotted against the relative pressure ($\triangle$P). The mixed gases were mixed at a 1:1 ratio. Flux for mixed gases is lower, primarily due

to the feed flow for single gases is 10 mL/min and for mixed gases it is 5 mL/min $CO_2$ and 5 mL/min $N_2$, therefore 10 mL/min in total.

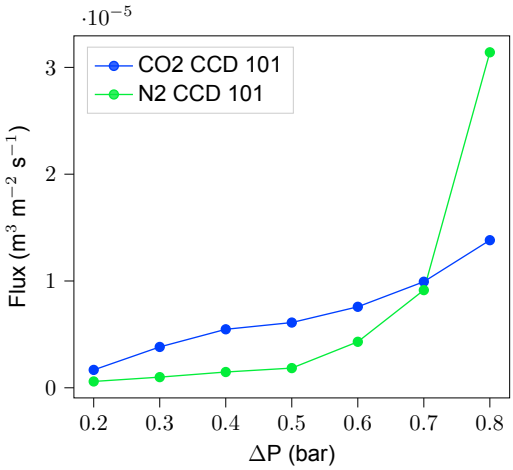


**Figure 4.9:** Single gas flux on CCD 101. Flux increases together with a relative pressure increase. The bubble point is around 0.6 bar, the point which the pores become opened and no separation occurs.

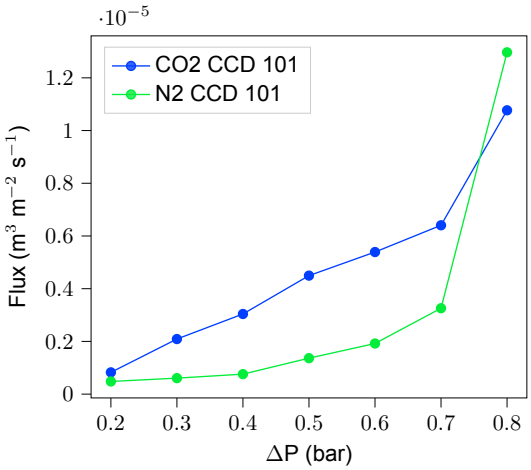


**Figure 4.10:** 1:1 ratio mixed gas flux on CCD 101. Flux increases together with a relative pressure increase. The bubble point is around 0.6 bar, the point which the pores become opened and no separation occurs.

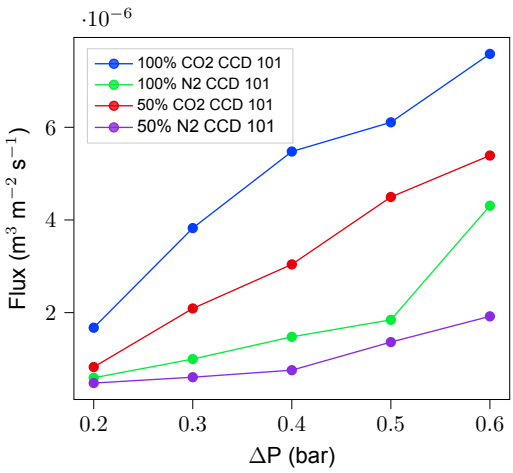


**Figure 4.11:** Single & Mixed gas flux on CCD 101 before breakthrough. Flux for mixed gases is lower, primarily due to the feed flow for single gases is 10 mL/min and for mixed gases it is 5 mL/min $CO_2$ and 5 mL/min $N_2$. The trend between single and mixed gases is the same. 50% $CO_2$ indicates that 50% is $CO_2$ and the other 50% is $N_2$.

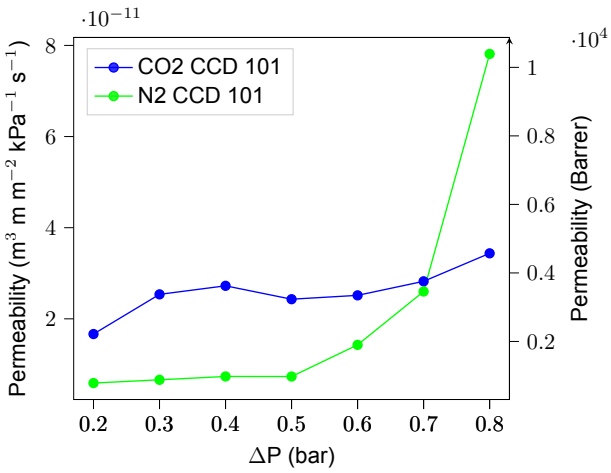


**Figure 4.12:** Single gas permeability on CCD 101. There is an overall increase in permeability as the relative pressure increases. The measurements for CO2 CCD 101 of 0.5, 0.6 and 0.7 bar were performed on another date than the other CO2 CCD 101 measurements, therefore these values can contain a higher degree of error.

An increase in pressure has a positive effect on the flux of all gases. Added to this, $CO_2$ has higher flux than $N_2$ with single gas and also mixed gas. The bubble point, which is the pressure which the largest pores are opened, appears to be around 0.6 bar. This can be seen as the moment before a dramatic increase in flux. Due to the pores being opened, less separation occurs and the difference in how much $CO_2$ or $N_2$ becomes less. Using equation 4.1, the predicted bubble point for CCD 101 is $0.446 \pm 0.043$ bar, which does not correlate well with experimental values. The First Bubble Pore (FBP) size used was the average of all 3 runs, therefore including the large inhomogeneity. It can be reasoned that the section of the membrane used for CCD 101 has a pore distribution different than those measured with capillary flow porometry.

It should be noted the $CO_2$ single gas flux in Figure 4.9 at $\triangle P$ = 0.5, 0.6 & 0.7 was measured on different days than all other data points due to the back-pressure regulator being incorrectly handled and increased the relative pressure up to 0.8 bar, which is past the bubble point. This is also relevant for the

permeability results, shown in Figure 4.12 & 4.13. The permeability increases as the relative pressure increases, however it takes a different trend around 0.5, 0.6 and 0.7 bar. As discussed earlier, this can be attributed to the fact that this was done on a different day and is subject to the daily fluctuations of the MFC's. This trend is not seen in any other run that has been performed in a single day, such as the mixed gas experiments (Figure 4.13).

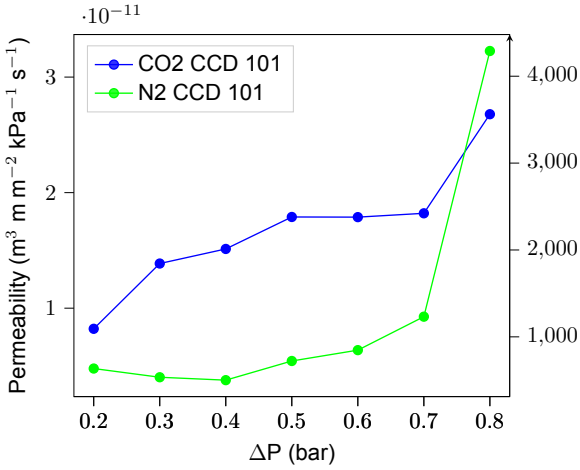


**Figure 4.13:** 1:1 ratio mixed gas permeability on CCD 101. Follows similar trend to that of single gases.

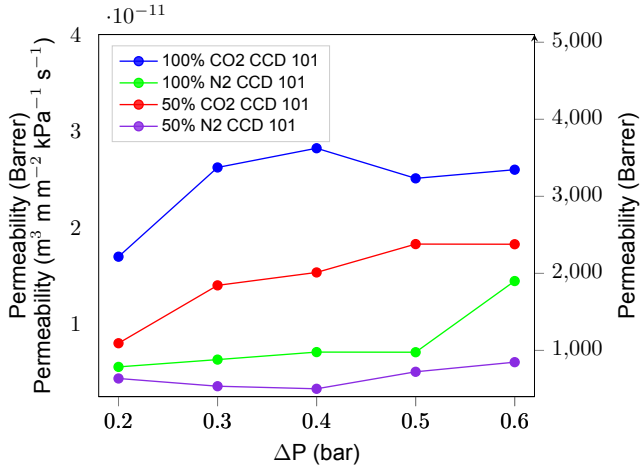


**Figure 4.14:** Single & Mixed gas permeability on CCD 101 before breakthrough pressure. 50% $CO_2$ indicates that 50% is $CO_2$ and the other 50% is $N_2$.

When the ideal and real selectivity of $CO_2$ over $N_2$ is plotted against relative pressure increase (Figure 4.15), it is seen that pressure increase has a positive effect on both kinds of selectivities. However, it peaks out at 0.3 bar for the ideal selectivity and at 0.4 bar for the real selectivity. However, once it gets close to the bubble point, it starts to drop dramatically. This is due to the pores being opened and less separation occurring and therefore leading to lower selectivity. An interesting thing of note is at 0.8 bar the selectivity drops slightly below 1, meaning the membrane permeates $N_2$ preferentially over $CO_2$. Despite $N_2$ having a larger kinetic diameter (364 pm) than $CO_2$ (330 pm), and therefore $N_2$ has a smaller mean free path (refer back to equation 2.8) and will collide more than $CO_2$, more $N_2$ permeates the membrane.

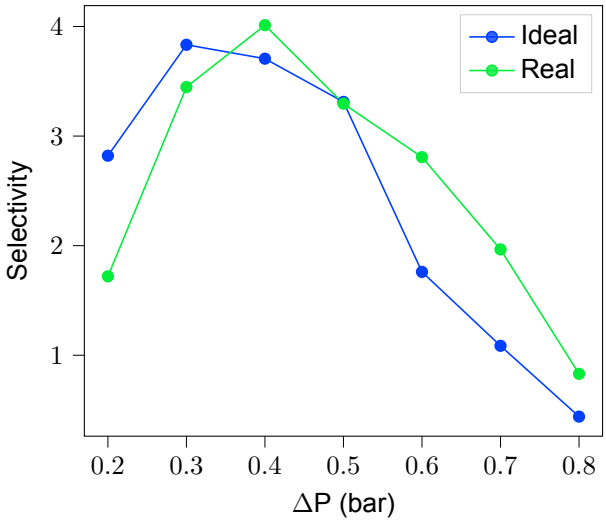


**Figure 4.15:** Ideal and real selectivity of $CO_2$ over $N_2$ against $\triangle$P on CCD 101. Both selectivities resemble eachother considerably.

When the same experiments were performed on CCD 102 (Figure 4.16, 4.18 & 4.19), the flux on CCD 102 is about equal for low pressures (0.2, 0.3 bar) as that of CCD 101. However, the flux is considerably larger at higher pressures (>0.4 bar). Another thing that is observed is that the bubble point occurs significantly earlier for CCD 102 than CCD 101. This is believed to be because of the inhomogeneity of the membranes, as the membrane used for the CCD 102 experiments was different than that of CCD 101. It was attempted to remove the Krytox 101 infused in membrane used for CCD 101 with acetone, however acetone had allowed the membrane to swell and the membrane had shrunk, therefore the membranes structure had been altered and could not be used for further experiments. The theoretical bubble point of CCD 102 is 0.438 $\pm$ 0.038 bar, not very different than that of CCD 101. This is to be

expected as both Krytox 101 and Krytox 102 are chemically very similar, both being fluorinated polymeric oils, only different in chain length. This leads to a difference in viscosity ($\eta_{101}$ = 25.4 mPa s and $\eta_{102}$ = 62.5 mPa s at 20 °C [16, 17]), density ($\rho_{101}$ = 1.89 g mL$^{-1}$ and $\rho_{102}$ = 1.91 g mL$^{-1}$ at 0 °C) and as previously mentioned, the surface tension (Table 4.2). The experimental bubble point of CCD 102 resembles its theoretical bubble point very well, approximately 0.4 bar and 0.438 bar respectively.

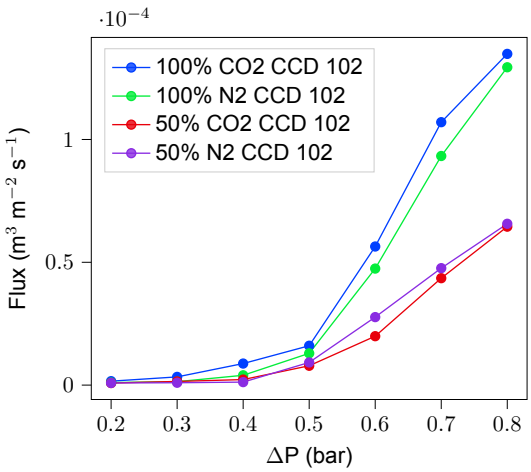


**Figure 4.16:** Single & Mixed gas Flux on CCD 102. The bubble point pressure is observed at 0.4 bar. 50% $CO_2$ indicates that 50% is $CO_2$ and the other 50% is $N_2$. A very low breakthrough pressure is observed.

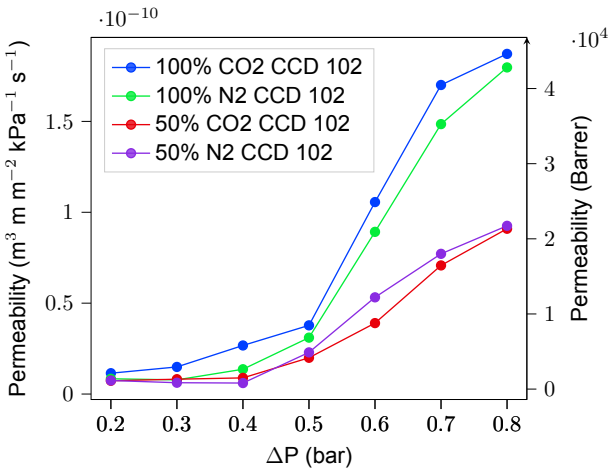


**Figure 4.17:** Single & Mixed gas permeability on CCD 102 before breakthrough pressure. 50% $CO_2$ indicates that 50% is $CO_2$ and the other 50% is $N_2$.

The permeabilities of CCD 102 is shown and compared to CCD 101 in Figure 4.20 & 4.21. Similar differences are seen as those discussed with the flux of CCD 101 and CCD 102. An interesting thing of note is that the $N_2$ permeability does not surpass that of $CO_2$ in the single gas experiments pressure range, however $N_2$ permeability does surpass $CO_2$ in the mixed gas experiments after the bubble point. This is reflected in the ideal and real selectivities. Shown in Figure 4.22, both types of selectivity peak prior to the bubble point and then drop. The ideal selectivity hovers above 1, meanwhile the real selectivity drops beneath it. The peak selectivity for CCD 102 ($\alpha_{ideal}$ = 2.40, $\alpha_{real}$ = 1.85) is also considerably less than that of CCD 101 ($\alpha_{ideal}$ = 3.83, $\alpha_{real}$ = 4.01), also shown in Figure 4.23, which can be attributed to the imperfections within the membrane or perhaps a lower solubility and/or diffusivity of $CO_2$ in Krytox 102 compared to Krytox 101.

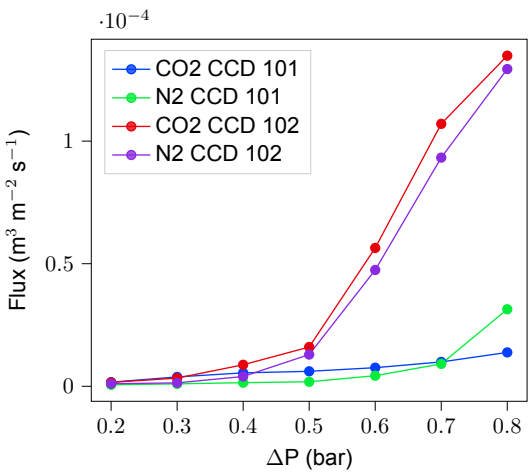


**Figure 4.18:** Single gas flux on CCD 102 compared with CCD 101. CCD 102 has much higher flux and a much earlier bubble point than that of CCD 101. Considerably higher fluxes for CCD 102 than for CCD 101.

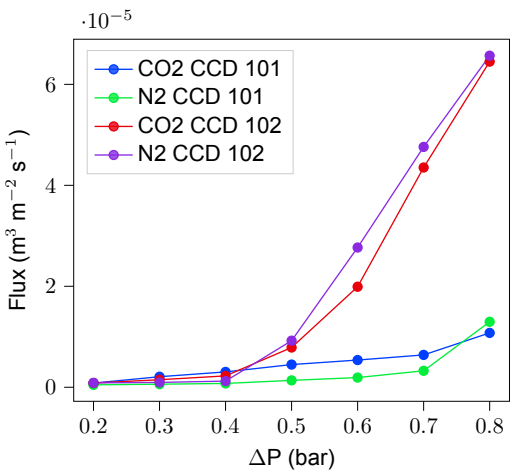


**Figure 4.19:** 1:1 ratio mixed gas flux on CCD 102 compared with CCD 101.

**Table 4.2: Physical properties of Krytox 101 & Krytox 102.**

| Physical Properties | Krytox 101 | Krytox 102 |
|---|---|---|
| Viscosity, $\eta$ (mPa s) (20 °C) | 25.4 | 62.5 |
| Density, $\rho$ (g mL$^{-1}$) (0 °C) | 1.89 | 1.91 |
| Surface Tension, $\gamma$ (mN m$^{-1}$) | 16.3 $\pm$ 0.13 | 15.35 $\pm$ 0.18 |

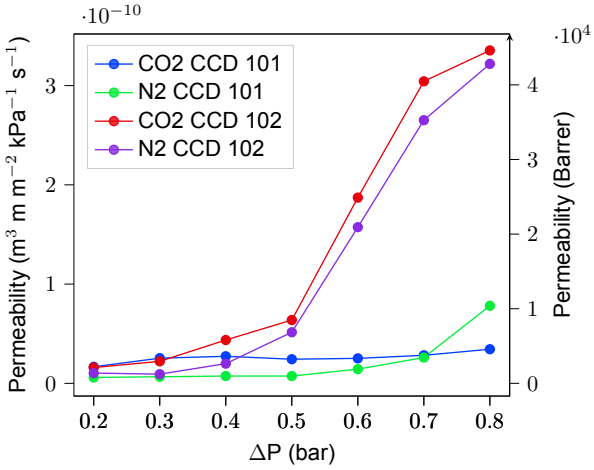


**Figure 4.20:** Single gas permeability on CCD 102 compared with CCD 101.

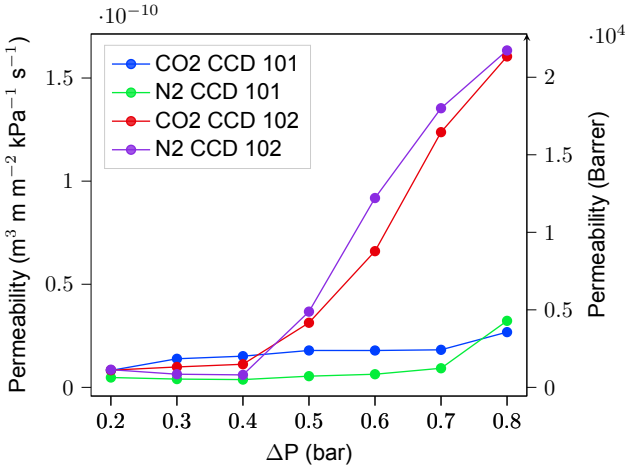


**Figure 4.21:** 1:1 ratio mixed gas permeability on CCD 102 compared with CCD 101.

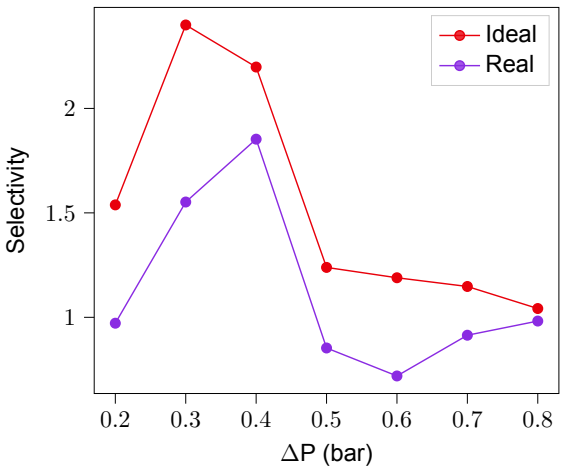


**Figure 4.22:** Ideal and real selectivity of $CO_2$ over $N_2$ against $\triangle$P on CCD 102. Both follow the same trend, with slightly differing values.

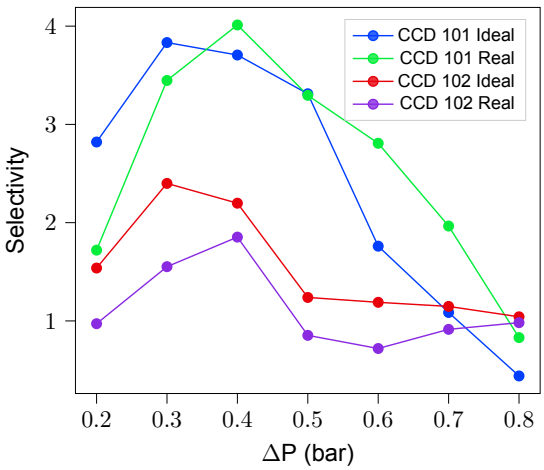


**Figure 4.23:** Ideal and real selectivity of $CO_2$ over $N_2$ against $\triangle$P on CCD 102 compared to CCD 101. Lowered selectivity is observed for CCD 102.

For the CCDs membrane infused with Krytox 101, the bubble point was not observed (Figure 4.24). This is due two linked reasons, the first is that the pores are considerably smaller than that of CCD, and therefore it requires higher pressures to force the oil out of the pores, with the theoretical bubble point for CCDs being 1.455 $\pm$ 0.074 bar. The second is that at higher pressures, the pressure regulator becomes increasingly more sensitive and difficult to control, which almost leaves it up to chance on whether the pressure desired will be the one that the feed reaches. Breakthrough was observed at very high pressures, however this data is shown in the Appendix and not in this section.

In stark contrast to CCD 101 & CCD 102, pressure increase has had a negative effect on the permeability of CCDs 101 (Figure 4.25). With increasing pressure, the permeability drops. A possible explanation for this phenomena is the closure of pores. With pressure increase, membrane gets compressed and the pore radius decreases slightly, reducing the surface area on the membrane surface for gas molecules to dissolve on, and possibly creating a more tortuous path for dissolved molecules to

diffuse through. A similar phenomena was observed by Song et al., where the permeability of Darcy's law did not follow a linear relationship with pressure increase [30]. They proposed a model that incorporated pressure induced deformation. It is possible that this pressure induced compression occurs in all membranes, however in the case of CCDs 101, the pores are small enough that the compression becomes significant enough to decrease the permeability. When comparing the fluxes of CCDs 101 with CCD 101 in Figure 4.26, the rate of flux increase in CCDs 101 is considerably less than that of CCD 101. It is also seen that the starting flux of CCDs 101 at 0.2 bar is higher than that of CCD 101, which would require more testing to validate and exclude possible errors.

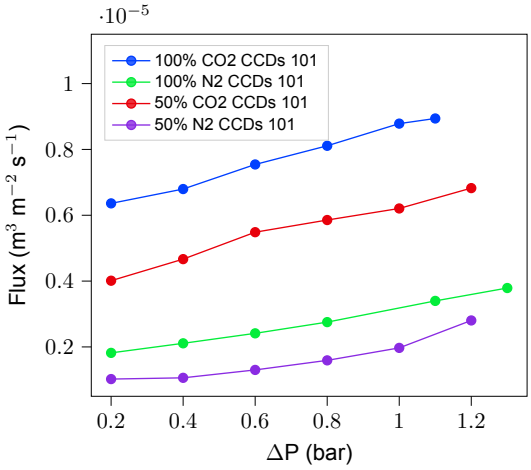


**Figure 4.24:** Single & Mixed gas Flux on CCDs 101. The bubble point pressure is observed at 0.4 bar. 50% $CO_2$ indicates that 50% is $CO_2$ and the other 50% is $N_2$.

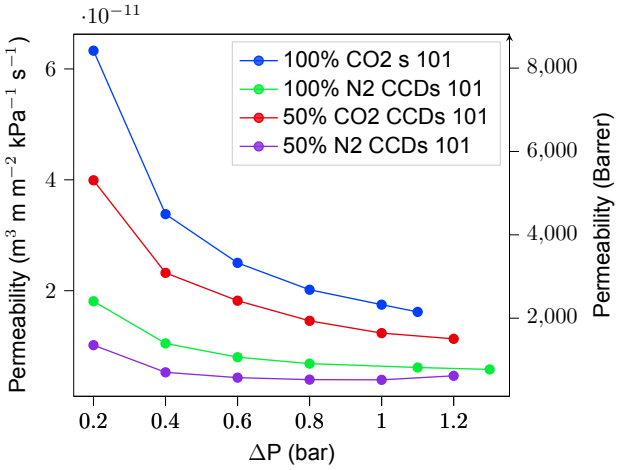


**Figure 4.25:** Single & Mixed gas Permeability on CCD 102. The bubble point pressure is observed at 0.4 bar. 50% $CO_2$ indicates that 50% is $CO_2$ and the other 50% is $N_2$.

In Figure 4.27, it is shown that the real selectivity outperforms the ideal selectivity for CCDs 101. The ideal selectivity starts at 3.5 and gently declines with a pressure increase, meanwhile the real selectivity peaks out at 0.4 bar and thereon follows a similar trend as the ideal selectivity. No plausible explanation for this can be thought of currently, this phenomena and the decrease of permeability with pressure increase phenomena warrants more investigation. The peak selectivities for all 3 used membranes are shown in Table 4.3, where Krytox 101 appears to be better than Krytox 102 by this data, however this is not conclusive and needs more data to back it up.

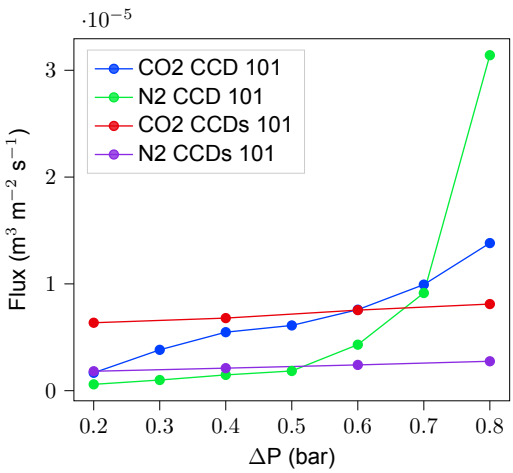


**Figure 4.26:** Single gas flux on CCDs 101 compared with CCD 101.

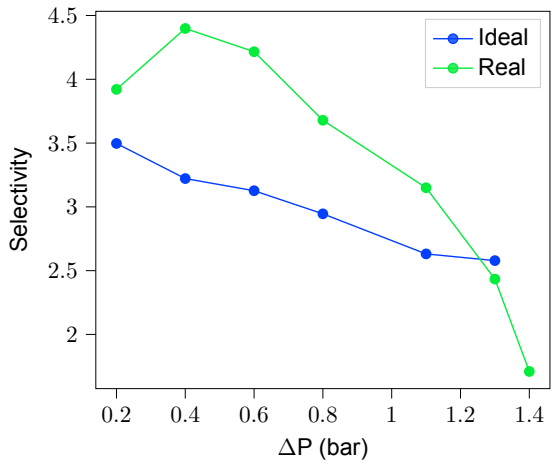


**Figure 4.27:** Ideal and real selectivity of $CO_2$ over $N_2$ against $\triangle$P on CCDs 101.

**Table 4.3: Peak selectivity of single & mixed gases for CCD 101, CCD 102 and CCDs 101.**

| Peak selectivity | CCD 101 | CCD 102 | CCDs 101 |
|---|---|---|---|
| Ideal | 3.95 | 2.40 | 3.50 |
| Real | 4.01 | 1.85 | 4.40 |

**$CO_2$ SOLUBILITY EXPERIMENTS**

The solubility curves found by the modified pressure decay method are plotted out in Figure 4.28 for Krytox 101 and Figure 4.29 for Krytox 102. The pressure unit bara stands for absolute pressure in bar.

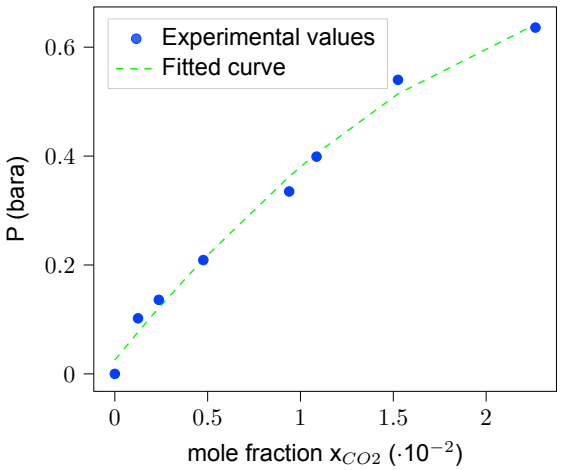


**Figure 4.28:** Solubility curve of Krytox 101, with absolute pressure P as a function of the mole fraction x of $CO_2$. A 2nd order polynomial is fitted and is shown as the dashed line. The Henry's constant is the limit slope of the fitted curve as $x_{CO_2} \to 0$.

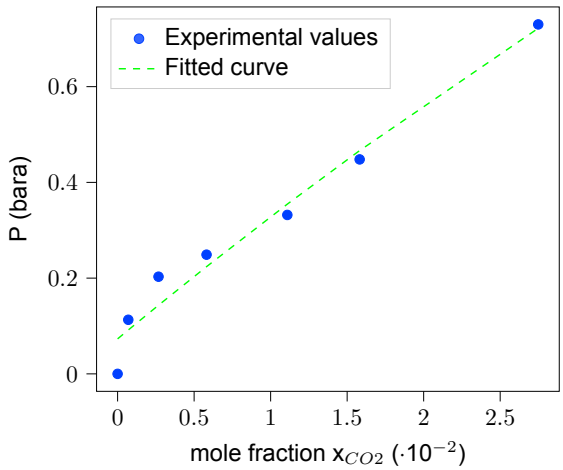


**Figure 4.29:** Solubility curve of Krytox 102, with absolute pressure P as a function of the mole fraction x of $CO_2$. A 2nd order polynomial is fitted and is shown as the dashed line. The Henry's constant is the limit slope of the fitted curve as $x_{CO_2} \to 0$.

Both measured solubility curves do not follow a linear relationship, therefore the solution of $CO_2$ and Krytox 101/102 are non-ideal. This is to be expected as fluorinated polymeric oils and carbon dioxide are very different in properties. The obtained limit slope as $x_{CO_2} \to 0$ (infinite dilution) for Krytox 101 is 4204.2 kPa (42.04 bar) and for Krytox 102 is 2657.9 kPa (26.58 bar). These limit slopes are therefore also the infinite dilution Henry's constant. Based off of this data, Krytox 102 has better dissolving ability of $CO_2$ than Krytox 101, which could suggest higher $CO_2$ permeability and/or $CO_2$ over $N_2$ selectivity for Krytox 102 supported-liquid membranes. A lower $k_H$ means a higher solubility, as is mathematically illustrated in equation 4.2:

$$x = \frac{P}{k_H} \tag{4.2}$$

If the pressure is kept constant, a larger value for $k_H$ will lead to a smaller value for the mole fraction x, which means less solute dissolved in the solvent.

Before continuing on it is once again important to discuss the ways error can occur, and why this data can't be trusted until these errors have been eliminated. First of all, the system is not adiabatic, which creates temperature gradients throughout the system. It was observed that the solvent was at the desired temperature of 30 °C, however the $CO_2$ temperature was lower by a few degrees. It could be assumed that the $CO_2$ at the gas-liquid interface is at 30 °C as well, and therefore at equilibrium the $CO_2$ dissolved is that of $CO_2$ at 30 °C. However, considering the setup measures the amount of gaseous $CO_2$ prior and after the liquid injection, these temperature gradients can give faulty measurements as to how much $CO_2$ is still in the gaseous state, and therefore also faulty measurements into how much $CO_2$ is in the solution. This can be circumvented by adding thermal insulation to the vessel and thereby making it adiabatic. Secondly, the Krytox oils used were sitting in an ambient environment prior to injection, therefore they can contain dissolved air prior to injection. This can create errors in the data, especially at lower pressures (<0.4 bar), as air can desorb from the Krytox oil and increase the pressure of the system, thereby allow an underestimation of the total $CO_2$ dissolved. This error can be circumvented by

degassing the Krytox oil prior to bringing it in contact with $CO_2$, however with the current set-up build this is not possible. This is however possible with the setup improvements provided in the Appendix. Thirdly, throughout the build of the setup and measuring, leaks were a consistent problem with the setup. The system needs to be completely isolated from the environment for accurate measurements. However leaks did not appear to be present in all measurements, as with higher pressure measurements (>0.6 bar) the system was left to run overnight, and a pressure decrease was observed and followed by a stable pressure. A lot of effort was put into eliminating all the sources of leaks, and the measurements used for this thesis did not have any leaks that could be detected by a gas leak detector spray, however a minuscule leak could not be completely ruled out. With all these significant errors, it is believed that this data is not trust worthy to draw accurate conclusions.
The Henry's constant of $CO_2$ in the Krytox oils at 30 °C derived from PC-SAFT modelling by Thijs van Westen from the Institute of Thermodynamics and Thermal Process Engineering at the University of Stuttgart are shown in Figure 4.30 & 4.31.

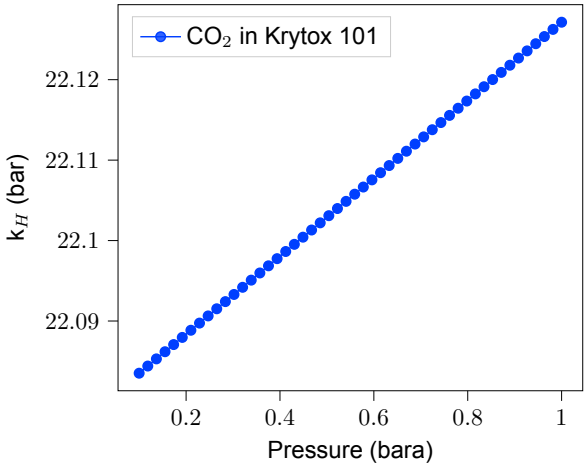


**Figure 4.30:** Henry's constant of $CO_2$ 30 °C in Krytox 101 at different pressure steps attained from PC-SAFT modelling. As is seen, pressure does not have a strong effect on the Henry's constant in these pressure ranges.

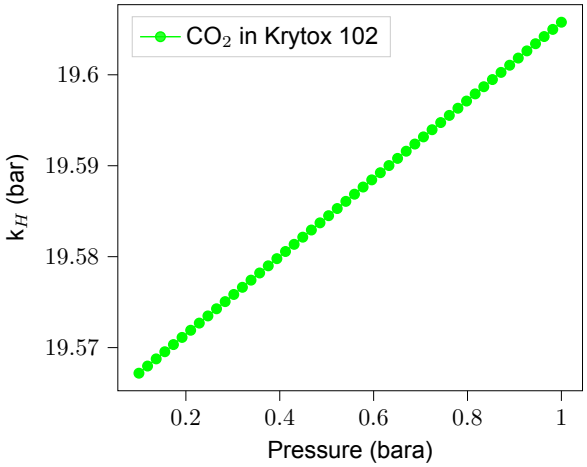


**Figure 4.31:** Henry's constant of $CO_2$ at 30 °C in Krytox 102 at different pressure steps attained from PC-SAFT modelling. As is seen, pressure does not have a strong effect on the Henry's constant in these pressure ranges. The solubility values of Krytox 102 are lower than that of Krytox 101.

An increasing pressure has a positive effect on the Henry's constant for both Krytox 101 and Krytox 102, however this effect is limited within the pressure ranges shown. What is also shown is that the Henry's constant values for Krytox 102 are lower than that of Krytox 101, similar to the experimental data. For the pressure effect on the experimental solubility, taking the slope of the polynomial fit over different pressure steps in Figure 4.28 & 4.29, the experimental solubility as a function of pressure can be calculated and is shown in Figure 4.32 & 4.33.

The theoretical data predicts that with increasing pressure, less $CO_2$ dissolves into the Krytox oils, which can suggest a decrease in permeability with pressure increase. In contrast, the experimental data predicts that with increasing pressure, more $CO_2$ dissolves into the Krytox oils, which could then lead to an increase in permeability as the pressure increases. For comparison, the Henry constants at infinite dilution for the theoretical and experimental data is shown in Table 4.4.

**Table 4.4: Experimental and theoretical values for Henry's constant of Krytox 101 and Krytox 102 at infinite dilution.**

| $k_H$ (kPa) | Krytox 101 | Krytox 102 |
|---|---|---|
| Experimental | 4204.2 | 2657.9 |
| Theoretical | 2207.9 | 1956.3 |

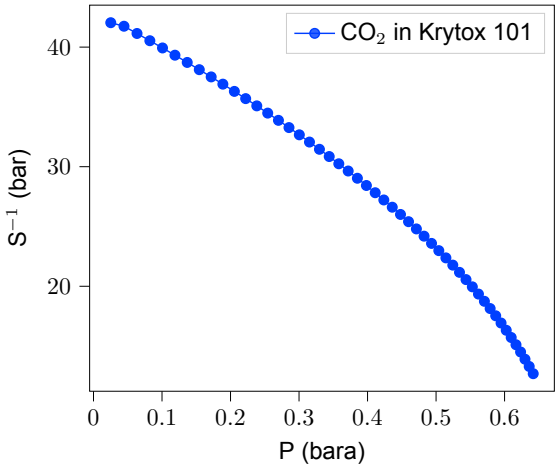


**Figure 4.32:** Inverse solubility ($S^{-1}$) of $CO_2$ 30 °C in Krytox 101 as a function of pressure attained from $CO_2$ solubility experiments.

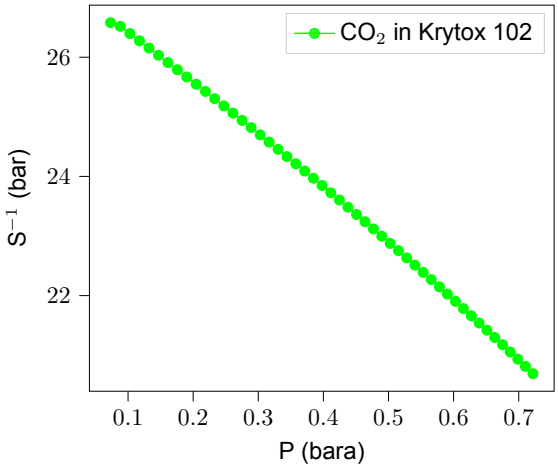


**Figure 4.33:** Inverse Solubility ($S^{-1}$) of $CO_2$ 30 °C in Krytox 101 as a function of pressure attained from $CO_2$ solubility experiments.

The experimental values are much higher than the theoretical, a factor of 1.90 higher for Krytox 101 and 1.36 higher for Krytox 102. This does not discredit the PC-SAFT model however, due to the possible errors in the experimental data discussed earlier. What is clear however, is that Krytox 102 has a higher solubility for $CO_2$ than Krytox 101.

**$CO_2$ DIFFUSION COEFFICIENT**

It is well known that the diffusion coefficient is a function of pressure, with increasing pressure typically leading to increased diffusion of solutes [7]. However in this work, the diffusion coefficient is assumed to remain constant in the pressure ranges that have been explored with the gas separation experiments. The diffusion coefficient is estimated using the Stokes-Einstein equation [12]:

$$D_i = \frac{k_B T}{6\pi\eta_i r_i} \tag{4.3}$$

Where $\eta_i$ is the viscosity of compound i and $r_i$ is the radius of compound i. The viscosity of the Krytox oils at 20, 40 and 70 °C are shown in Table 4.5.

**Table 4.5: Viscosity of Krytox 101 and Krytox 102 as a function of temperature.**

| Viscosity $\eta$ (mPa s) | Krytox 101 | Krytox 102 |
|---|---|---|
| 20 °C | 25.4 | 62.5 |
| 40 °C | 12.5 | 27.6 |
| 50 °C | 9.3 | 19.4 |
| 70 °C | 5.6 | 10.5 |

For most liquids, viscosity does not possess a linear relationship with temperature, however the following relation can be used to estimate the viscosity [6]:

$$log(\eta) = A + \frac{B}{T} + C \cdot T + D \cdot T^2 \tag{4.4}$$

Using the data in Table 4.5, the regression coefficients A, B, C and D are estimated and shown in Table 4.6.

**Table 4.6: Regression coefficients for estimating viscosity of Krytox 101 and Krytox 102.**

| Coefficients | Krytox 101 | Krytox 102 |
|---|---|---|
| A | -25.878 | -18.378 |
| B (K) | 4064.14 | 3386.8 |
| C ($K^{-1}$) | 0.0615588 | 0.038976 |
| D ($K^{-2}$) | -0.000053867 | -0.000032667 |

The calculated viscosity of Krytox 101 and Krytox 102 at 30 °C are 17.45 mPa s and 40.75 mPa s respectively, which are in agreement with the experimental values of 17.46 mPa s for Krytox 101 and 40.55 mPa s for Krytox 102. The radius $r_i$ used is the kinetic diameter of $CO_2$ divided by two, therefore $r_{CO2}$ 165 pm. Using the Stokes-Einstein relation (equation 4.3, the diffusion coefficient ($D_i$) of $CO_2$ at 30 °C in Krytox 101 and Krytox 102 is calculated to be $7.73 \cdot 10^{-11}$ $m^2$ $s^{-1}$ and $3.32 \cdot 10^{-11}$ $m^2$ $s^{-1}$ respectively. Due to the higher viscosity of Krytox 102, its diffusion coefficient for $CO_2$ is lower than that of Krytox 101. This can lead to a lower permeability that is predicted by the solution-diffusion model. These values are however very low, especially when it is compared with $CO_2$ diffusion coefficients measured by an in-house magnetic suspension balance ($2.84 \cdot 10^{-9}$). Due to the inability of the current solubility setup to measure the diffusion coefficient and still needing a diffusion coefficient, it is assumed that $D_i$ is 1000 times the Stokes-Einstein diffusionc coefficient. Therefore the $D_i$ chosen in this work for Krytox 101 and Krytox 102 are $7.73 \cdot 10^{-8}$ $m^2$ $s^{-1}$ and $3.32 \cdot 10^{-8}$ $m^2$ $s^{-1}$ respectively.

**$CO_2$ PERMEABILITY**

As was described in the Transport Model section of this work, permeability ($Pe$) is the product of solubility and diffusivity , shown in equation 2.16. Using the experimental and theoretical solubilities and the assumed diffusion coefficient, the permeability can be calculated:

$$Pe = S \cdot D_i \tag{4.5}$$

The permeabilities obtained from the gas experiments (CCD 101, CCDs 101 & CCD 102) are plotted together with the permeabilities obtained from the experimental and theoretical solubility values in Figure 4.34 & 4.35.

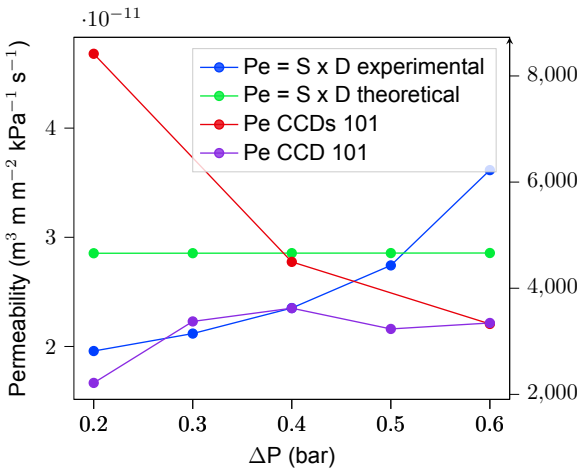


**Figure 4.34:** Permeabilities of $CO_2$ at through a Krytox 101 infused membrane obtained from gas experiments and calculations at 30 °C. Pe = S x D experimental is the permeability attained by using experimental values for solubility, Pe = S x D theoretical is the permeability attained by using theoretical values for solubility, Pe CCDs 101 is the permeability attained from gas experiments on CCDs 101 and Pe CCD 101 is the permeability attained from gas experiments on CCD 101. None of the values of any source agree with one another.

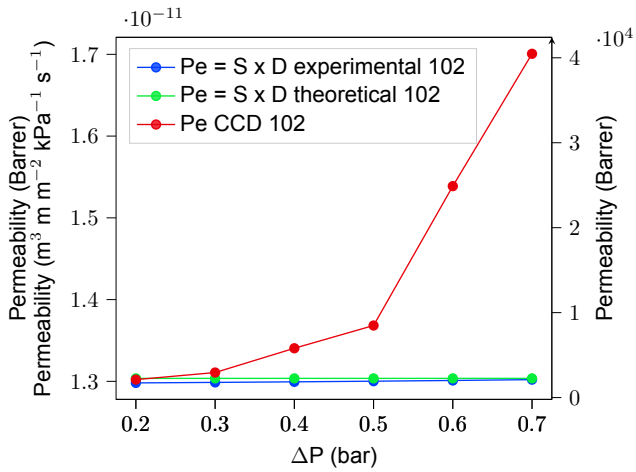


**Figure 4.35:** Permeabilities of $CO_2$ at through a Krytox 102 infused membrane obtained from gas experiments and calculations at 30 °C. Pe = S x D experimental is the permeability attained by using experimental values for solubility, Pe = S x D theoretical is the permeability attained by using theoretical values for solubility and Pe CCD 102 is the permeability attained from gas experiments on CCD 102.

These two graphs are to compare the permeability obtained from different methods, with the goal being that the permeability values calculated using equation 4.5 closely resemble the permeability values found through the gas experiments such as the CCD 101, CCDs 101 and CCD 102 permeabilities. If this is the case, solution-diffusion model correctly describes gas flow through the Krytox infused membranes.

The permeability obtained from experimental Krytox 101 solubility data closely resembles the permeability (Figure 4.34). The trend is similar in that the permeability increases with pressure increase. It should once again be mentioned that the permeability values of CCD 101 at 0.5 and 0.6 bar of relative

pressure were measured on a different date than the preceding permeability values, therefore it likely contains a small error. If the diffusion coefficient is assumed to be correct, this is strong evidence that solution-diffusion model is the model CCD 101 follows. With the improvements to the solubility given in the Appendix, it will be possible to attain the solubility and diffusivity with much higher accuracy.
The permeability obtained from theoretical solubility data decreases with pressure increase, however it is weakly affected by a pressure increase. This incorrectly describes the permeability trends seen in the gas permeation experiments.
In Figure 4.35, neither the permeabilities calculated with experimental or theoretical data correctly describe the permeability measured with CCD 102. However with the CCD 102 experiments, it is believed that large membrane defects were present and therefore the solution-diffusion model is unlikely to fully describe CCD 102. In Figure 4.36, the experimentally and theoretically calculated permeabilities of $CO_2$ are better shown to not agree with each other in trend, however their values are not drastically different with a maximum difference of 23.6% at 0.2 bar. The trends however do not correlate well with each other.

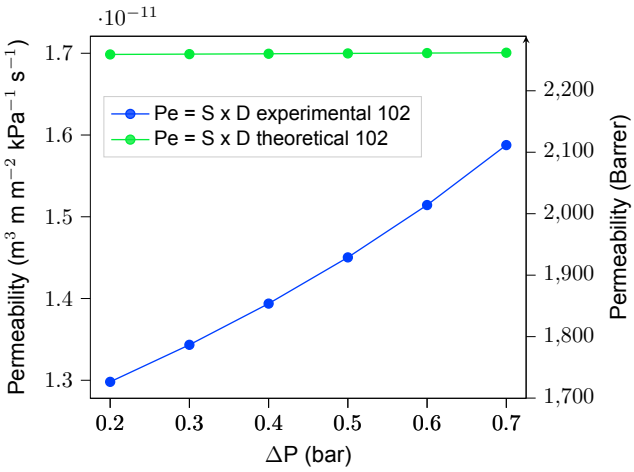


**Figure 4.36:** Permeabilities of $CO_2$ at through a Krytox 101 and Krytox 102 infused membranes obtained from calculations at 30 °C. Pe = S x D experimental 101 is the permeability attained by using experimental values for solubility of Krytox 101, Pe = S x D experimental 102 is the permeability attained by using experimental values for solubility of Krytox 102 and Pe = S x D theoretical 102 is the permeability attained by using theoretical values for solubility of Krytox 102.

**CONVECTIVE FLOW**

A sign of convective flow through membranes is when the permeability scales together with a relative pressure increase linearly. One way to observe this is to take the logarithm of the permeability and pressure and plot them against each other, and if the slope of a certain region is equal to 1, it is scaling linearly and could suggest convective flow. This was done with the data from CCD 101, shown in Figure 4.37.
As is shown, the slope prior to breakthrough is 0.377, which suggests there is no convective flow occurring. At high pressures, the slope is 0.905, which could suggest convective flow. This would be logical, as a large amount of the pores have been opened and a bunch of convective flow occurs. However, these are only 3 data points, therefore it isn't enough to make decisive conclusions. In all other experiments, no convective flow was observed, which is evidence supporting that solution-diffusion model is correct for these membranes. There was one special case where there is good evidence for convective flow, with CCDs 101 $N_2$ single gas, shown in Figure 4.38.
The first out of the 5 data points is at 1.3 bar relative pressure, which is close to the theoretical bubble point of CCDs 101 (1.455 bar). These 5 data points definitely suggest convective flow, especially due to them being very close to the theoretical bubble point. If the $N_2$ solubility and diffusivity in Krytox 101 were available, it could be shown whether solution-diffusion with imperfections model does or does not apply to the membrane in this region.

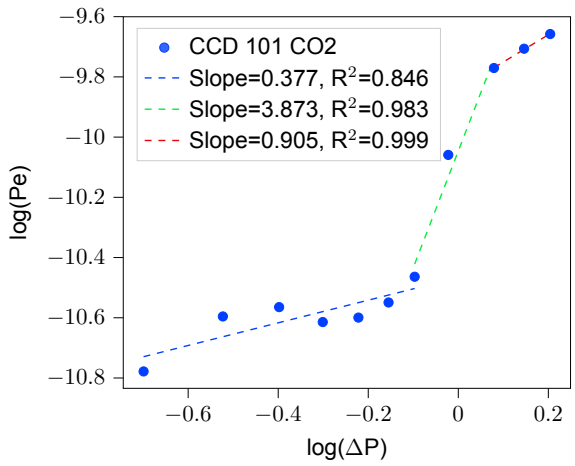


**Figure 4.37:** Logarithm of permeability of CCD 101 $CO_2$ single gas and relative pressure plotted against each other. The slope in the solution-diffusion region (prior to breakthrough) is not 1, therefore suggest that it does not have any convective flow.

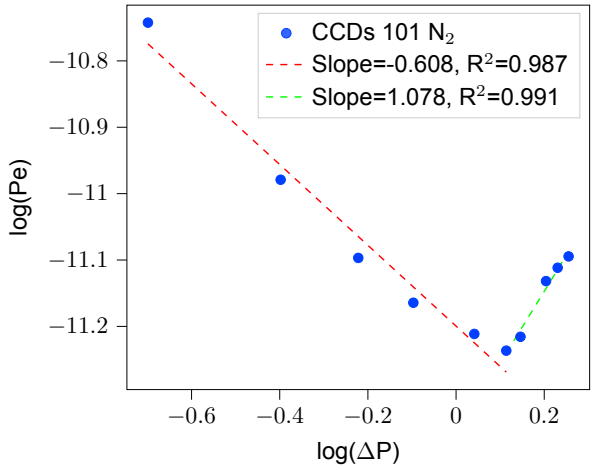


**Figure 4.38:** Logarithm of permeability of CCDs 101 $N_2$ single gas and relative pressure plotted against each other. The slope at pressures 1.3 bar and higher have a slope of 1.078.

# 5 Conclusion

In this work, the gas transport through Krytox oil infused membranes was investigated. It was observed that the membranes had a higher permeability for $CO_2$ over $N_2$, with the permeability increasing with a relative pressure increase in all membranes except CCDs 101. This selectivity of $CO_2$ over $N_2$ was observed in ideal and real settings. Furthermore, it was shown that selectivity is also a function of pressure, with a peak selectivity approximately a pressure step before the bubble point, the pressure at which the liquids within the pores are pushed out and are therefore opened. It was also shown that pore size play a significant role in gas permeation with the membranes. Defects in the pores can lower the bubble point, and shorten the operable pressure ranges for these membranes. The mean pore size also plays a significant role, it was shown that CCDs 101, a membrane with small pore sizes wetted with Krytox 101 had its permeability decrease as the relative pressure increased. It is hypothesized that all membrane are being compressed as the pressure increases, however CCDs 101's pores are small enough that the compression is significant enough to reduce the permeability.
Based on the data acquired with the solubility experiments, $CO_2$ solubility in Krytox oils increases with an absolute pressure increase, and if the diffusion coefficient is assumed to be constant, the permeability predicted by the solution-diffusion model will also increase with pressure. This is what was observed via the gas experiments, however the values of permeability are not in agreement with one another. It was also shown that the solubility of $CO_2$ in Krytox 102 is higher than that of $CO_2$ in Krytox 101. However as was discussed, there are many sources of error with this data and therefore this data can't discredit the solution-diffusion model. The theoretical solubility data obtained by PC-SAFT modelling predicts a decrease in solubility with absolute pressure increase, which when a constant diffusion coefficient is assumed, predicts a decreasing permeability with pressure increase, which is in large disagreement with the gas experiments performed on CCD 101 and CCD 102. The trend might be in agreement with CCDs 101, however it was shown in previous work that pressure induced deformation can play a significant role in the permeability through membranes. It was once again shown that the solubility of $CO_2$ in Krytox 102 is higher than that of $CO_2$ in Krytox 101 by the PC-SAFT modelling. The values for the solubility of $CO_2$ obtained via experimental and theoretical means are in disagreement with one another as well, however with Krytox 102 the largest difference in values between the two is 24.5%. Considering the unreliability of the data, this work is not able to discredit the solution-diffusion model and therefore unable to determine which model best suits these Krytox oil infused membranes.

**Recommendations for future work**

For future work, performing the $CO_2$ solubility experiments in an improved setup will show which model best describes these supported liquid membranes. Measuring the solubility of $N_2$ and other gases in the oils can further show which model suits these membranes best. Further studies on the effects of pressure on membranes, specifically relating to permeability increases and decreases depending on the pore sizes is also recommended. Lastly, testing out new liquids such as Ionic Liquids and Deep Eutectic Solvents in supported liquid membranes is also of interest.

# 6

# Acknowledgements

I would like to give out my thanks to Prof. **Atsushi Urakawa** for allowing me to be part of the Catalysis Engineering group and use the gas permeation setup in their lab. I would also like to thank **Liliana Baron** for teaching me how to use the gas permeation setup and teaching me the calculations surrounding it. I would like to thank Dr. **Vatsal Shah** for fabricating and providing the PVDF membranes. I would like to thank Dr. **Mahinder Ramdin** for supplying me with the materials and parts neccesary for the low pressure solubility setup. I would also like to thank Dr. **Thijs van Westen** for providing the theoretical solubility data. Lastly, I would like to thank Dr. **Hanieh Bazyar** for allowing this Bachelor End Project to happen.

# References


[1] Mahsa Akbari and Peyvand Valeh-e-Sheyda. “CO2 equilibrium solubility in and physical properties for monoethanolamine glycinate at low pressures”. In: *Process Safety and Environmental Protection* 132 (2019), pp. 116–125. DOI: 10.1016/j.psep.2019.10.003.

[2] Jennifer L. Anthony, Edward J. Maginn, and Joan F. Brennecke. “Solubilities and thermodynamic properties of gases in the ionic liquid 1-n-butyl-3-methylimidazolium hexafluorophosphate”. In: *The Journal of Physical Chemistry B* 106.29 (2002), pp. 7315–7320. DOI: 10.1021/jp020631a.

[3] Richard W. Baker. *Membrane Technology and applications*. McGraw-Hill, 2000.

[4] Hanieh Bazyar et al. “Liquid–liquid displacement in slippery liquid-infused membranes (SLIM’s)”. In: *Soft Matter* 14.10 (Feb. 2018), pp. 1780–1788. DOI: 10.1039/c7sm02337e.

[5] Joseph D. Berry et al. “Measurement of surface and interfacial tension using pendant drop tensiometry”. In: *Journal of Colloid and Interface Science* 454 (2015), pp. 226–237. DOI: 10.1016/j.jcis.2015.05.012.

[6] A. Kayode Coker. “Physical properties of liquids and gases”. In: *Ludwig’s Applied Process Design for Chemical and Petrochemical Plants* (2007), pp. 103–132. DOI: 10.1016/b978-075067766-0/50010-5.

[7] J. S. Collura et al. “The effects of concentration, pressure, and temperature on the diffusion coefficient and correlation length of SDS Micelles”. In: *The Journal of Physical Chemistry B* 105.21 (2001), pp. 4846–4852. DOI: 10.1021/jp004572h.

[8] Daniel Fierro, Adriana Boschetti-de-Fierro, and Volker Abetz. “The solution-diffusion with imperfections model as a method to understand organic solvent nanofiltration of multicomponent systems”. In: *Journal of Membrane Science* 413-414 (2012), pp. 91–101. DOI: 10.1016/j.memsci.2012.04.027.

[9] Karel Friess et al. “A review on Ionic liquid gas separation membranes”. In: *Membranes* 11.2 (2021), p. 97. DOI: 10.3390/membranes11020097.

[10] IPCC. *Climate Change 2021: The Physical Science Basis. Contribution of Working Group I to the Sixth Assessment Report of the Intergovernmental Panel on Climate Change*. Cambridge University Press, 2021. URL: https://www.ipcc.ch/report/ar6/wg1/.

[11] IPCC. *Global warming of 1.5°C. An IPCC Special Report on the impacts of global warming of 1.5°C above pre-industrial levels and related global greenhouse gas emission pathways, in the context of strengthening the global response to the threat of climate change*. Cambridge University Press, 2018. URL: https://www.ipcc.ch/sr15/.

[12] Yoshiki Ishii, Tomohiro Murakami, and Norikazu Ohtori. “Molecular size and shape effects: Tracer diffusion and the stokes-einstein relation”. In: *Journal of Molecular Liquids* 346 (2022), p. 118235. DOI: 10.1016/j.molliq.2021.118235.

[13] N.M. Kocherginsky, Qian Yang, and Lalitha Seelam. “Recent advances in supported liquid membrane technology”. In: *Separation and Purification Technology* 53.2 (2007), pp. 171–177. DOI: 10.1016/j.seppur.2006.06.022.

[14] Anjaneya Sarma Kovvali. “Immobilized liquid membranes for facilitated transport and gas separation”. In: *Disserations* (May 2001).

[15] Matthias M. Krejca. “Recent advances in gas separation via supported liquid membranes”. In: *Multidisciplinary Advances in Efficient Separation Processes* (Jan. 2020), pp. 37–71. DOI: 10.1021/bk-2020-1348.ch002.

[16] *Krytox™ GPL101 Oil*. https://www.chempoint.com/products/chemours/krytox-oils/krytox-oils-for-general-purpose-applications/krytox-gpl101-oil. Accessed: 11-04-2022.

[17] *Krytox™ GPL102 Oil*. https://www.chempoint.com/products/chemours/krytox-oils/krytox-oils-for-general-purpose-applications/krytox-gpl102-oil. Accessed: 11-04-2022.

[18] Mingcan Mei et al. "CO2 capture by 1-ethyl-3-methylimidazolium acetate: Solubility at low pressure and quantification of chemisorption and physisorption". In: *Journal of Molecular Liquids* 348 (2022), p. 118036. DOI: 10.1016/j.molliq.2021.118036.

[19] Endre Nagy. "Membrane contactors". In: *Basic Equations of Mass Transport Through a Membrane Layer* (2019), pp. 337–345. DOI: 10.1016/b978-0-12-813722-2.00011-x.

[20] George A. Olah, Alain Goeppert, and G. K. Surya Prakash. "Chemical Recycling of Carbon Dioxide to Methanol and Dimethyl Ether: From Greenhouse Gas to Renewable, Environmentally Carbon Neutral Fuels and Synthetic Hydrocarbons". In: *The Journal of Organic Chemistry* 74.2 (2009). PMID: 19063591, pp. 487–498. DOI: 10.1021/jo801260f. URL: https://doi.org/10.1021/jo801260f.

[21] George A. Olah, G. K. Surya Prakash, and Alain Goeppert. "Anthropogenic Chemical Carbon Cycle for a Sustainable Future". In: *Journal of the American Chemical Society* 133.33 (2011). PMID: 21612273, pp. 12881–12898. DOI: 10.1021/ja202642y. URL: https://doi.org/10.1021/ja202642y.

[22] *Porometry, bubble point and liquid permeability characterization. POROMETER, www.porometer.com*. Apr. 2022. URL: https://www.porometer.com/.

[23] J.F. RICHARDSON, J.H. HARKER, and J.R. BACKHURST. "Flow of fluids through granular beds and packed columns". In: *Chemical Engineering* (2002), pp. 191–236. DOI: 10.1016/b978-0-08-049064-9.50015-1.

[24] Lloyd M. Robeson. "Correlation of separation factor versus permeability for polymeric membranes". In: *Journal of Membrane Science* 62.2 (1991), pp. 165–185. ISSN: 0376-7388. DOI: https://doi.org/10.1016/0376-7388(91)80060-J. URL: https://www.sciencedirect.com/science/article/pii/037673889180060J.

[25] Lloyd M. Robeson. "The upper bound revisited". In: *Journal of Membrane Science* 320.1 (2008), pp. 390–400. ISSN: 0376-7388. DOI: https://doi.org/10.1016/j.memsci.2008.04.030. URL: https://www.sciencedirect.com/science/article/pii/S0376738808003347.

[26] Paul Scovazzo et al. "Supported ionic liquid membranes and facilitated ionic liquid membranes". In: *ACS Symposium Series* (Jan. 2002), pp. 69–87. DOI: 10.1021/bk-2002-0818.ch006.

[27] Vatsal Shah, Bo Wang, and Kang Li. "High-performance PVDF membranes prepared by the combined crystallisation and diffusion (CCD) method using a dual-casting technique: A breakthrough for water treatment applications". In: *Energy & Environmental Science* 14.10 (2021), pp. 5491–5500. DOI: 10.1039/d1ee02009a.

[28] T. K. Sherwood, P. L. Brian, and R. E. Fisher. "Desalination by reverse osmosis". In: *Industrial & Engineering Chemistry Fundamentals* 6.1 (1967), pp. 2–12. DOI: 10.1021/i160021a001.

[29] Emma L. Smith, Andrew P. Abbott, and Karl S. Ryder. "Deep eutectic solvents (DESS) and their applications". In: *Chemical Reviews* 114.21 (2014), pp. 11060–11082. DOI: 10.1021/cr300162p.

[30] Ryungeun Song et al. "Pressure-driven flow across a hyperelastic porous membrane". In: *Journal of Fluid Mechanics* 871 (2019), pp. 742–754. DOI: 10.1017/jfm.2019.298.

[31] Petr Uchytil et al. "Description of the gas transport through dynamic liquid membrane". In: *Separation and Purification Technology* 184 (2017), pp. 152–157. DOI: 10.1016/j.seppur.2017.04.014.

[32] Sílvio Vaz, Ana Paula Rodrigues de Souza, and Bruno Eduardo Lobo Baeta. "Technologies for carbon dioxide capture: A review applied to energy sectors". In: *Cleaner Engineering and Technology* 8 (2022), p. 100456. ISSN: 2666-7908. DOI: https://doi.org/10.1016/j.clet.2022.100456. URL: https://www.sciencedirect.com/science/article/pii/S2666790822000611.

[33] Lawrence K. Wang et al. *Membrane and desalination Technologies*. Humana Press, 2011.

[34] William J. Ward and Walter L. Robb. "Carbon dioxide-oxygen separation: Facilitated transport of carbon dioxide across a liquid film". In: *Science* 156.3781 (1967), pp. 1481–1484. DOI: 10.1126/science.156.3781.1481.

[35] J.G. Wijmans and R.W. Baker. “The solution-diffusion model: a review”. In: *Journal of Membrane Science* 107.1 (1995), pp. 1–21. ISSN: 0376-7388. DOI: https://doi.org/10.1016/0376-7388(95)00102-I. URL: https://www.sciencedirect.com/science/article/pii/0376738895001021.

[36] John X.J. Zhang and Kazunori Hoshino. “Microfluidics and Micro Total Analytical Systems”. In: *Molecular Sensors and Nanodevices* (2014), pp. 103–168. DOI: 10.1016/b978-1-4557-7631-3.00003-x.

# A

# Appendix

**Scanning Electron Microscopy**

Electron microscopy has a much higher resolution than light microscopy, primarily due to the use of electron beams instead of light beams. Electrons exhibit wave characteristics, allowing it to have very small wavelengths in comparison to visible light. This leads to a very high resolution, able to see the surfaces of many materials with good detail.

Scanning Electron Microscopy (SEM) uses a focused electron beam on a compound, usually coated with vaporized gold or palladium ions. The coated compound is moved back and forth and left to right, allowing the electron beam to strike the entire surface, essentially scanning the surface of the compound. This yields an image with 3-dimensional characteristics such as capillaries and deformities. The electrons in the electron beam (primary electrons) collide with the electrons of the surface atoms, releasing them from their orbitals (Figure A.1). These released electrons are known as secondary electrons, which are picked up by a detector and the image is processed.

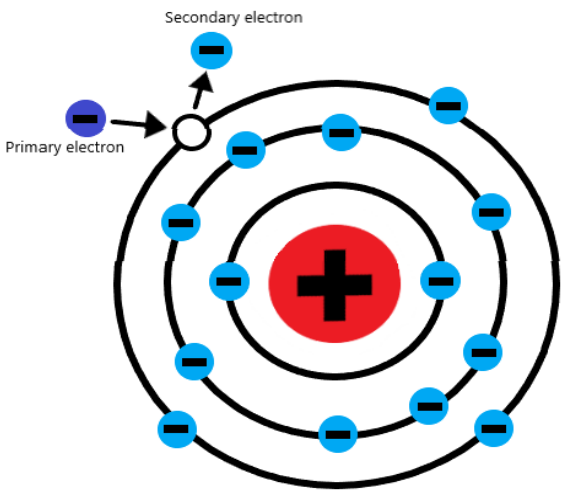


**Figure A.1:** Primary electron colliding with electron within orbital, releasing it and creating a secondary electron

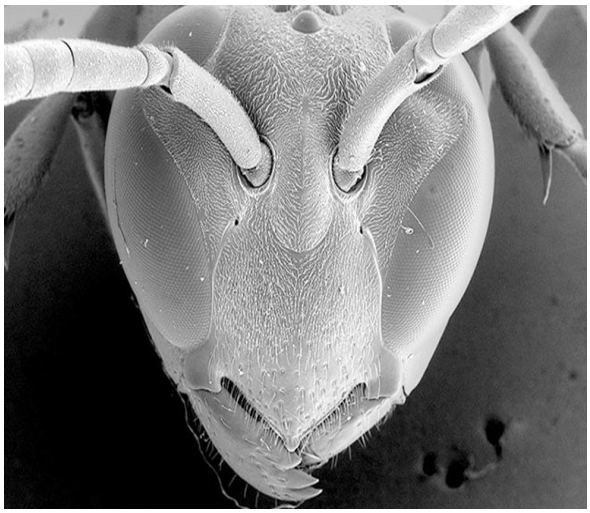

**Figure A.2:** SEM image of a bee head. (Reproduced from the Nature article "In pictures: details revealed with advanced SEM")

Examples of SEM images are those shown in the Results & Discussion (Section 4). Others are a 2 mm bee head in Figure A.2 and main reproductive organ (sporangium) of a mould species in Figure A.3.

**Contact Angle**

The contact angle ($\theta$) is the angle that occurs at an interface between a liquid and a solid. It is a measure for the attractive interactions between the two phases, where the larger the contact angle;

the less attracted the two phases are to eachother. When $\theta$ < 90 °, the surface is considered wettable by the liquid, and there is attraction between the solid and liquid. When $\theta$ > 90 °, there is repulsion between the two phases and the surface is considered non-wettable (Figure A.5). It must be noted that the wettability is not only determined by the solid, but also by the liquid composition. In the case of water as the liquid, $\theta$ < 90 ° is hydrophilic, $\theta$ > 90 ° is hydrophobic and $\theta$ > 150 ° is known as superhydrophobic.

**Figure A.3:** SEM image of main mould reproductive organ, known as a sporangium. (Reproduced from the Nature article "In pictures: details revealed with advanced SEM")

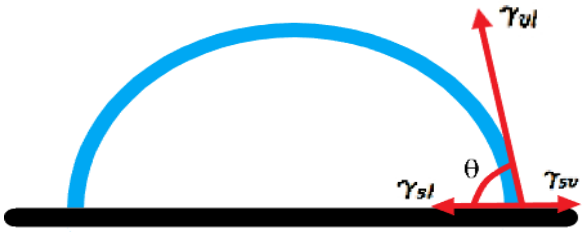


**Figure A.4:** Surface tension between the 3 phases, $\gamma_{sl}$ is between the solid and liquid, $\gamma_{sv}$ is between the solid and vapor, $\gamma_{vl}$ is between the vapor and liquid.

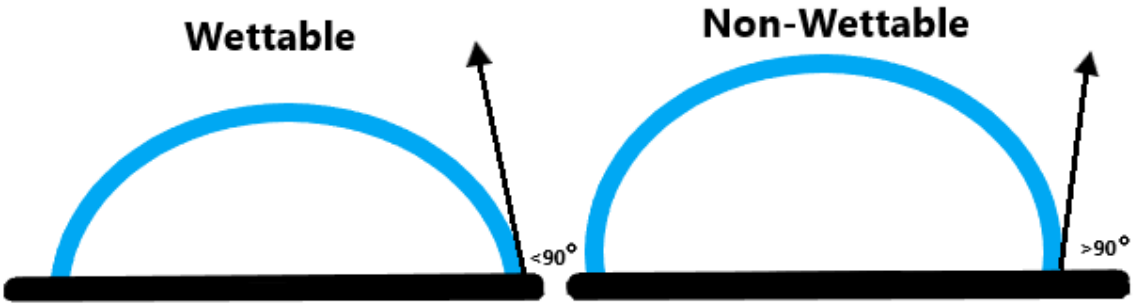


**Figure A.5:** Contact angles of a wettable surface (< 90 °) and a non-wettable surface (> 90 °).

Fundamentally, the attractive forces arise from the electrostatic interaction between (hydrogen bonds or van der Waals) molecules, leading to cohesion (same molecules attracted to eachother) or adhesion (different molecules attracted to eachother). Whether the two phases attract eachother at the interfaces determines the surface energy (surface tension), where having a high surface energy between eachother means having little attraction, leading to a bigger contact angle (Figure A.4). When the surface tensions are in equilibrium, the bubble will form in the shape of its contact angle (assuming a smooth and uniform surface).

Young's equation reveals the relation between the 3 surface energies together with the contact angle, this being:

$$\gamma_{sv} = \gamma_{sl} + \gamma_{lv} \cdot \cos(\theta) \tag{A.1}$$

Young's equation can be seen as a force balance, where at equilibrium the forces cancel each other out to yield net zero. $\theta$ used in this case is the advancing contact angle.

***Static & Dynamic CA***

The static CA is when the contact angle is measured at once the droplet is in equilibrium. The dynamic CA is measured by changing the droplet size continuously over many cycles. The advancing dynamic CA is the angle measured when the droplet size is increased and the receding dynamic CA is the angle when the droplet size is increased. The difference between the advancing and receding angle is known as the hysteresis, which is a measure of how ”slippery” the membrane is. The smaller the hysteresis, the slipperier the membrane. In the case of dry hydrophobic membranes, the hysteresis is typically around 20°. In the case of liquid infused hydrophobic membranes, the hysteresis is typically around 5°.

**Pressure Stability**

Pressure stability stands for the pressure range where the fluid within wetted capillaries of a membrane have not been forced out. Capillary forces are what keep the fluid within the capillaries, however, when an external pressure applies a force exceeding the capillary forces, the fluid is pushed out of the capillaries. The equation governing capillary forces is known as the Young-Laplace equation:

$$\triangle P = \frac{2\gamma \cdot \cos(\theta)}{r} \tag{A.2}$$

$\triangle P$ is the pressure needed to push the liquid out (breakthrough pressure), $\gamma$ is the surface tension between the liquid and air, $\theta$ is the contact angle discussed in A and r is the pore radius. This equation assumes cylindrical pores, which is a good approximation for normal pores. With pressure stability tests, the pressure starts low and it slowly is increased until the liquid within the membrane is forced out. This can be seen as an abrupt and drastic increase of flux through the membrane.

**Capillary Flow Porometry**

Capillary Flow Porometry (CFP) is an analysis method used to calculate the pore size distribution within a membrane. When creating membranes, the pore radii will differ, leading to smaller and larger pores. In CFP, the gas flow rate through an unwetted membrane is measured starting at low pressure and increases in small increments, this yields the dry curve (Figure A.6). The same procedure is done with a wetted membrane. Similar to pressure stability tests, the liquid within the membrane will be pushed out once the capillary forces have been exceeded. However in CFP, first the liquid through the larger pores are pushed out (larger pores have a larger radius, thus lower breakthough pressure). The pressure is further increased to push the liquid out of the smaller pores. The result of these events is shown in the wet curve (Figure A.6), where the largest pores correspond to the first breakthrough pressure (otherwise known as first bubble point (FBP)), and the smallest pores correspond to the pressures of the wet-curve and dry-curve intersection. The mean flow pore (MFP) is the pore size related to the mean flow, which is at the intersection of the wet curve and the half dry curve. Using the different breakthrough pressures and the Young-Laplace equation (eq. A.2), the pore size distribution can be calculated (graphically shown in Figure A.7), and from there the mean pore size of the membrane as well. The half-dry curve is calculated using the mean pore size.

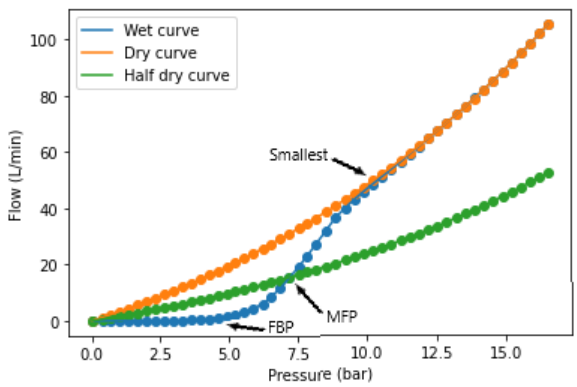


**Figure A.6:** Capillary Flow Porometry results of the CCD PVDF membrane. The dry, wet and half-dry curves are indicated with different shapes.

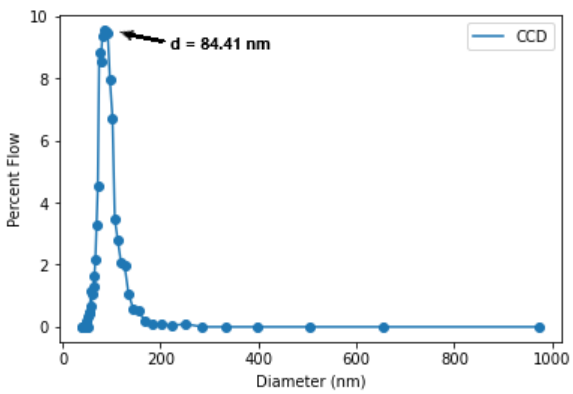


**Figure A.7:** Pore size distribution obtained via Capillary flow porometry of the CCD PVDF membrane. The mean pore size is 91.08 nm.

**Gas Chromatography**

Gas Chromatography (GC) is an analysis technique reliant on sample volatility. The main parts of a GC is the **oven**, **column** and the **detector**, which is schematically shown in Figure A.8. A GC can measure the concentrations in a sample by firstly evaporating the sample, secondly separating the components within the sample in a chromatography column and lastly detection of the individual components within the sample. Compounds that are unstable upon evaporation can not be used in a GC. In the case of gas separation, no phase changes must occur for the use of a GC as the compounds are permanent gases. The gas is injected and is accompanied by a carrier gas known as the mobile phase. The carrier gas is $He$ in most cases. However, in the case of $H_2$, $Ar$ should be used as $H_2$ and $He$ are very similar in properties, leading to inaccurate detection. The sample is brought into the GC column, where the sample comes in contact with the stationary phase. The stationary phase is a material that is coated onto the column walls. Separation occurs via the different affinities of the gases to the stationary phase. The oven, column and detector are briefly discussed in the following sections.

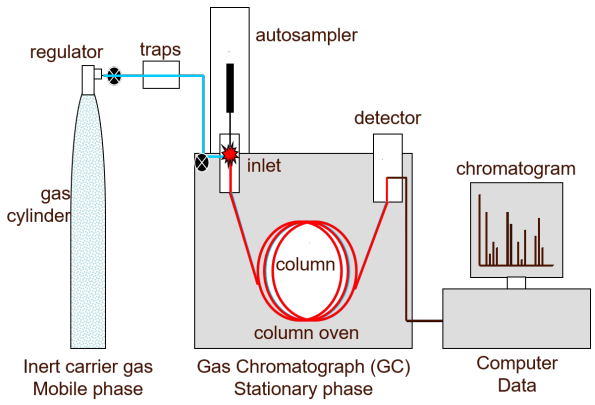


**Figure A.8:** Schematic representation of a Gas Chromatography setup. In this case the Mass Spectrometer (MS) functions as the detector. Reproduced from "Gas Chromatography – How a Gas Chromatography Machine Works, How To Read a Chromatograph and GCxGC"

***Oven***

A critical step when using GC is choosing the temperature the column has to be at. This is done via an oven which can ensure a constant temperature throughout the entire separation run (isothermal), or the temperature can be programmed to increase at certain rates throughout the run. Changing the column temperature can ensure increased separation in cases where many compounds with a wide range of boiling points are present. In cases of simple gas separation this is not necessary, the column can be run isothermally.

***Column***

As was previously mentioned, separation occurs via the difference in affinity of the gas to the stationary phase. This affinity can be solubility into a highly viscous fluid functioning as the stationary phase, or it can be a high surface area molecular sieve functioning as a temporary holding cell for molecules. In case of a high viscous fluid, the lesser soluble gases will flow quickly through the column, meanwhile the components with higher solubility will tend to stick longer within the column. With the molecular sieves, larger molecules will be temporarily captured and stick longer in the column and the smaller molecules will be less impeded and therefore reach the detector quickly.

***Detector***

There are a large variety of detectors with a variety of different purposes, two of the most commonly used are outlined.

Thermal Conductivity Detectors (TCD's) are universal detectors, typically used for permanent gases and not for organic compounds. The detector is built out of two cells, where the gas from the column flows through one and a carrier gas is in the other as a reference. There are filaments present in the cells, when gases with different thermal conductivities to that of the carrier gas pass over the filaments, the temperature of the filament changes together with its electrical resistance. This change in electrical resistance is measured and is proportional to the difference in thermal conductivity between the carrier gas and analyte, allowing the detection of compounds present in the sample.

Flame Ionization Detectors (FID's) are used for detection of organic compounds as it responds to compounds with C-H bonds. The analyte is burned together with $H_2$ and Air on top of a flame jet. Two electrodes are set on both sides of the flame, a negative potential difference is applied between the two electrodes and the analytes are burned in the flame to produce ions and electrons. The electrons flow to the collector electrode, producing current which is amplified to produce a measurable signal. FID's are the most commonly used detector.

**Supplementary Graphs**

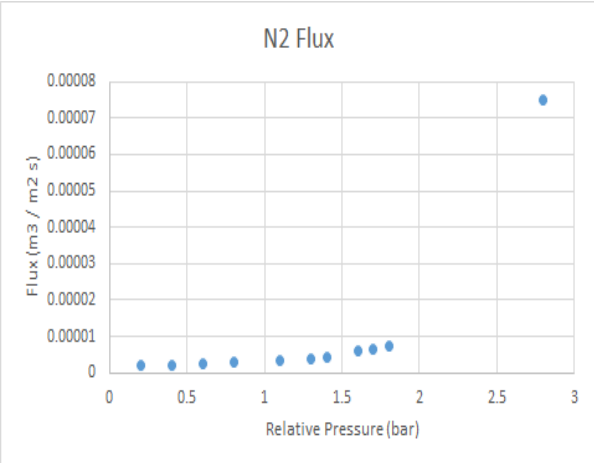


**Figure A.9:** Single gas $N_2$ flux as a function of relative pressure on **CCDs 101**. Breakthrough was observed at high pressures (2.8 bar).

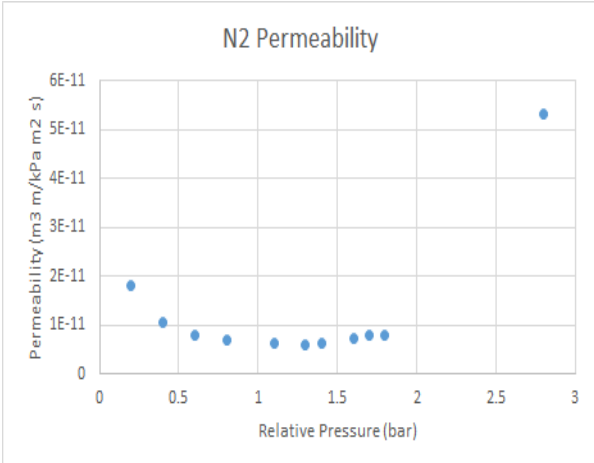


**Figure A.10:** Single gas $N_2$ permeability as a function of relative pressure on **CCDs 101**. Breakthrough was observed at high pressures (2.8 bar).

**VLE improvements**

Due to the many possible sources of errors, it is paramount to improve the setup to obtain reliable low pressure solubility data. The first improvement would be to have $CO_2$ sit in a separate adiabatic container fitted with a separate pressure sensor. This container will be heated to the desired temperature. This improvement has many positive effects on the setup, such as not needing time to equilibriate within the vessel, not needing to remove the liquid in between each experiment, allowing the ability to degas the liquid within the vessel by drawing a vacuum and having a more accurate readout of the initial amount of $CO_2$. The second improvement would be to thermally insulate the vessel and thereby removing the temperature gradients present within the setup. Lastly, although this is not an improvement

to the setup itself, is to get a better understanding about the software used for the pressure readout. A picture of the setup as it is currently without these improvements is shown in Figure A.11.

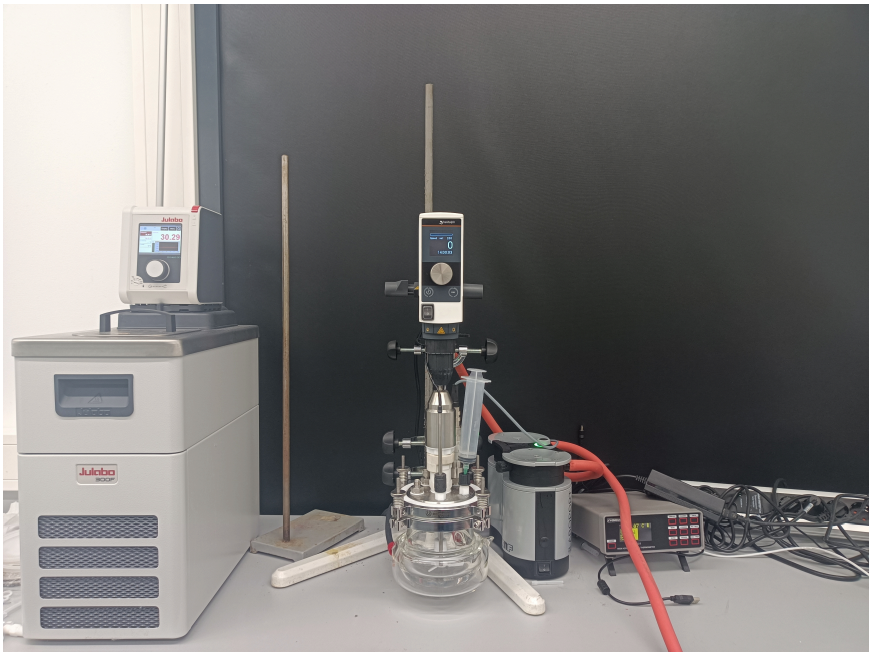


**Figure A.11:** Picture of the solubility setup without the $CO_2$ injection line being connected.